Electric Power Systems Research 250 (2026) 112169

Contents lists available at ScienceDirect

Electric Power Systems Research

journal homepage: www.elsevier.com/locate/epsr

Adaptive multi-objective real-time hierarchical control for isolated microgrid clusters utilizing an enhanced particle swarm optimization strategy to optimize costs and emissions

Pablo Horrillo-Quintero [a], Pablo García-Triviño [a], David Carrasco-González [a], Raúl Sarrias-Mena [b], Marcos Tostado [c], Francisco Jurado [c], Luis Sainz Sapera [d], Luis M. Fernández-Ramírez [a,*]

[a] Research Group in Sustainable and Renewable Electrical Technologies (PAIDI-TEP023), Department of Electrical Engineering, Higher Technical School of Engineering of Algeciras (ETSIA), University of Cádiz, Avda. Ramón Puyol, s/n. 11202 Algeciras (Cádiz), Spain
[b] Research Group in Sustainable and Renewable Electrical Technologies (PAIDI-TEP023), Department of Engineering in Automation, Electronics and Computer Architecture & Networks, Higher Technical School of Engineering of Algeciras (ETSIA), University of Cádiz, Avda. Ramón Puyol, s/n. 11202 Algeciras (Cádiz), Spain
[c] Research Group in Research and Electrical Technology (PAIDI-TEP-152), Department of Electrical Engineering, EPS Linares, University of Jaén, C/Alfonso X, n 28, 23700, Linares (Jaén), Spain
[d] Department of Electrical Engineering, ETSEIB, UPC, Av. Diagonal 647, 08028 Barcelona, Spain

ARTICLE INFO

Keywords:
Isolated microgrid cluster
Multi-objective optimization
Hierarchical control
Adaptive droop control
Particle swarm optimization

ABSTRACT

This paper introduces an adaptive hierarchical control for an isolated microgrid cluster (IMGC) leveraging a real-time multi-objective particle swarm optimization (MOPSO) algorithm. It simultaneously considers CO_2 emissions minimization as a tertiary control objective and total losses minimization as a primary control objective, integrating grid-supporting and grid-feeding inverters for MG interconnection. The effectiveness of the MOPSO-based hierarchical control is demonstrated across multiple scenarios. Compared to a hierarchical control based on proportional power distribution relative to the rated inverter capacities of the MGs, the proposed method shows a 27.21% reduction in total losses and a 7.66% reduction in CO_2 emissions. When compared with an optimization based on the fmincon solver, the proposed approach achieves a 22.92% reduction in losses and a 3.5% decrease in emissions. Additionally, centralized secondary control improves MRE indices by 100.09%, ITAE by 28.5%, ITSE by 43.78%, IAE by 30.61%, and ITSE by 47.72%, compared to the primary control strategy based on proportional approach. The MOPSO approach demonstrates robustness and flexibility, maintaining stable frequency and voltage within set thresholds during MG failures and sudden demand changes. Finally, the practical feasibility of the proposed approach is verified in a hardware-in-the-loop experimental setup using an OPAL-RT4512 unit and a dSPACE MicroLabBox. The experimental results, utilizing a time step of 50 μs, are consistent with the simulation outcomes, ensuring voltage and frequency control as its rated references.

1. Introduction

Isolated microgrid clusters (IMGC) represent a promising solution for providing energy in remote areas or those disconnected from the main power grid. These systems consist of several interconnected microgrids (MGs) that can operate autonomously or collectively, enhancing the stability and resilience of the isolated network [1]. In this context, voltage and frequency control is essential to ensure power quality, preventing fluctuations that could affect the operation of sensitive equipment, and ensuring a reliable supply [2].

Effective voltage and frequency control in an IMGC is complex due to the variability of renewable generation, limitations in storage capacity, and load fluctuations [3]. Generally, MGs that incorporate a high proportion of distributed energy resources (DERs) based on power converters exhibit low inertia characteristics, which increases their susceptibility to experiencing significant voltage and frequency

* Corresponding author.
E-mail addresses: pablo.horrillo@uca.es (P. Horrillo-Quintero), pablo.garcia@uca.es (P. García-Triviño), david.carrasco@uca.es (D. Carrasco-González), raulsarrias@uca.es (R. Sarrias-Mena), mtostado@ujaen.es (M. Tostado), fjurado@ujaen.es (F. Jurado), luis.sainz@upc.edu (L.S. Sapera), luis.fernandez@uca.es (L.M. Fernández-Ramírez).

https://doi.org/10.1016/j.epsr.2025.112169
Received 20 December 2024; Received in revised form 28 July 2025; Accepted 25 August 2025
Available online 28 August 2025

fluctuations following a disturbance [4]. Therefore, advanced and updated control algorithms are required to ensure stable and cost-effective operation. In light of these challenges, a dynamic control approach is necessary, capable of responding in real-time, minimizing fluctuations, and optimizing the performance of MG clusters (MGCs), thereby ensuring stable and reliable operation [5]. Real-time control capabilities are essential for IMGC due to the inherent variability and uncertainty of DERs, such as renewable generation and fluctuating loads. These technologies require continuous monitoring and quick response to maintain stability, ensure power quality, and prevent outages in the absence of a main grid connection [6]. Unlike grid-connected systems, isolated MGs cannot rely on external support for frequency and voltage regulation, making real-time control indispensable for dynamically balancing supply and demand [7]. Furthermore, real-time control enables effective management of energy storage systems (ESSs) and demand response strategies, optimizing operational efficiency and extending component lifespan under variable conditions [8]. Recent studies have demonstrated that implementing real-time control frameworks significantly enhances the resilience and reliability of IMGC, especially when integrating intermittent DERs [9]. Therefore, advancing real-time control approaches is critical to achieving sustainable, reliable, and autonomous operation of IMGC.

In this context, the hierarchical control structure becomes essential, as it effectively addresses different levels of control [10]. Primary control in MGs is based on droop control [11]. However, this power-sharing method does not ensure the economic operation of the system. In [12], a hierarchical and distributed cooperative control strategy based on pinning was proposed for alternating current (AC) MGCs. To address the limitations of conventional droop control in power-sharing applications for capacitive-coupled inverters, authors in [13] proposed an innovative active-reactive power coupling strategy. It was examined how substantial coupling capacitance and the inherent decoupling in droop control significantly restricted the controllable power range, rendering its practical application challenging.

An adaptive active power droop controller and voltage setpoint control was developed in [14] for isolated MGs, focusing on optimizing frequency response and stability after disturbances. A similar study can be found in [15] where a centrifugal and gravitational search algorithm was used to address issues related to energy sharing with high inductive load, or in [16], where a controller based on droop and sliding mode was designed for energy sharing in an isolated direct current (DC) MG, utilizing an enhanced nonlinear droop model. In a higher level, the secondary control complements the task of primary control to improve the power quality inside MGs and to enhance the system performance by removing the steady-state errors of the frequency and voltage [17]. The tertiary control is responsible for establishing the optimal power dispatch. Normally, this power dispatch is based on minimizing a cost function primarily related to operational costs, CO_2 emissions, or efficiency [18]. A fully distributed hierarchical coordination controller was presented in [19], which minimized the global total generation cost in a DC MGC by managing the optimal power-sharing among them.

In isolated MGs, diesel generators often serve as distributed generation units to compensate for the intermittency and variability inherent to DERs [20]. Authors in [21] addressed sustainability in isolated MGs by proposing an energy management system (EMS) based on model predictive control (MPC), specifically designed to minimize greenhouse gas emissions. The system prioritized the use of renewable energy—primarily from a photovoltaic generator—while coordinating the operation of a diesel generator and a lithium-ion battery ESS (BESS). The study in [22] focused on reducing CO_2 emissions in isolated MGs through an optimized energy management approach. This approach controlled excess power generation and maximized renewable energy use, effectively minimizing reliance on conventional energy sources and leading to a substantial decrease in greenhouse gas emissions. The results highlighted how careful system design and operation can significantly enhance the environmental sustainability of isolated MG systems. Similarly, the work in [23] presented an approach to reducing CO_2 emissions in islanded MGs by integrating DERs with optimized thermal and electrical ESSs, achieving nearly a 50% reduction. Despite employing carbon capture and storage, achieving emission reduction in a cost-competitive approach remained challenging, underscoring the need for strategies that simultaneously reduce both costs and emissions.

An adaptive distributed economic control was proposed in [24] for isolated MGs. This approach introduced a droop control based on marginal costs and implemented adaptive consensus-based controllers to address storage capacity. Similarly, a distributed hierarchical control was implemented in [25] to minimize power losses in distribution, losses in the lines. The proposed control included a distributed gradient algorithm at the upper layer, consensus control at the secondary layer, and local droop control with a double-loop at the lower layer.

In IMGCs, minimizing both emissions and energy losses is essential to achieving a sustainable and resilient energy supply. Due to the absence of a main grid connection, any inefficiency in energy conversion or distribution directly impacts the system's reliability and operational cost, especially when dispatchable generators such as diesel units are involved [26]. While reducing losses improves technical performance, it does not necessarily guarantee a low environmental impact. Conversely, focusing solely on emissions reduction may overlook operational inefficiencies and compromise supply stability. Therefore, these two objectives must be addressed simultaneously and in a coordinated manner [27]. This joint optimization is particularly relevant when integrating DERs with variable generation patterns, where maintaining a balance between clean energy use and system efficiency becomes more complex [28]. Moreover, the limited availability of fuel and logistical constraints in remote areas make it imperative to adopt strategies that reduce fuel consumption while ensuring high energy utilization efficiency. Furthermore, it is uncommon to achieve simultaneous improvements in both emissions' reduction and loss minimization. Typically, enhancing one objective tends to compromise the other, due to inherent trade-offs in system operation and control strategies. For example, in [29], the cost associated with reducing emissions could be up to 250% higher.

Currently, granular ball computing (GBC) represents a promising computational paradigm aimed at improving optimization efficiency and adaptability in uncertain and data-rich contexts. Instead of relying on fixed-point representations, GBC employs adaptable granular regions that encapsulate local patterns and structural information, allowing for more scalable and flexible modeling of complex data distributions. Recent studies have extended the capabilities of GBC to address uncertainty and improve robustness in decision-making processes. For instance, in [30], a novel framework combining fuzzy rough sets and three-way decision theory was proposed to construct multilevel granular representations that dynamically adapt to data ambiguity. This method introduced a mechanism for distinguishing between confident and uncertain instances without relying on predefined risk thresholds, thereby enhancing classification under vague conditions. The proposed strategy further incorporated a sequential refinement of decisions and a criterion for selecting optimal granular spaces, enabling a more precise and resilient response to complex decision boundaries.

On the other hand, [31] explored the limitations of conventional granular-ball generation strategies in clustering applications, particularly those based on static thresholds or greedy heuristics. To overcome these issues, the authors proposed a method grounded in the principle of justifiable granularity. This method evaluated the quality of each granular ball using a metric that jointly considered its coverage and distinctiveness. This approach not only improved the alignment between the granular structures and the intrinsic distribution of the data, but it also incorporated mechanisms for anomaly detection that enhanced the reliability of the resulting clusters. Experimental evidence confirmed that the method yielded superior clustering performance compared to existing granular-ball-based and classical clustering techniques. These developments highlighted the strong potential of GBC to support advanced optimization methods by incorporating adaptive,

data-driven mechanisms for managing uncertainty and structural complexity—offering valuable pathways for future improvements in population-based metaheuristics algorithms.

Current research on hierarchical control of IMGCs exhibits the following limitations. Firstly, the simultaneous optimization of costs and emissions throughout the hierarchical control structure is not usually considered, [19,24,25], leading to suboptimal solutions in terms of sustainability and economic efficiency. Furthermore, there is a lack of strategies that take CO_2 emissions into account when distributing energy among MGs with different types of converters [32]. Additionally, there are not many simple and flexible methods available to minimize the total losses using droop control technique in IMGC [33]. Many control strategies lack real-time validation [34–36], which is essential to demonstrate their practical viability and computational efficiency.

In particular, references [34] and [35] introduced distributed hierarchical control strategies for AC MGCs. Their primary focus was on coordinating frequency and voltage regulation using iterative learning mechanisms, droop-based strategies, and sparse communication topologies. These contributions were valuable for ensuring distributed regulation of active and reactive power under communication constraints. However, their control objectives were limited to maintaining power balance and system stability. In contrast, the proposed work goes a step further by introducing a hierarchical control architecture embedded with a multi-objective optimization layer. This layer explicitly addresses the minimization of CO_2 emissions and distribution losses—two conflicting but highly relevant performance criteria in sustainable energy systems—objectives not considered in [34] and [35].

Moreover, while the strategies in [34] and [35] adopted layered control structures with pinning communication and time-scale separation, they did not account for real-time optimization of power sharing between MGs based on environmental and efficiency trade-offs. The technique designed in this paper, however, not only integrates optimization-driven decision-making at the tertiary control level but also leverages both GS (grid supporting) and GF (grid feeding) inverters for enhanced dynamic adaptability. This dual-inverter scheme enables robust and flexible interconnection of multiple MGs, allowing for coordinated operation even under MG failure conditions—an aspect not explored in [34] and [35]. In addition, although the aforementioned studies addressed sparse or low-bandwidth communication scenarios, they did not consider the effects of communication delays or loss of connectivity. This work includes an explicit analysis validated through real-time hardware in the loop (HIL) experiments, offering a level of practical demonstration that exceeded the simulation-based assessments reported in those references.

Compared to [36], which focused on a two-layer energy management framework for a single islanded MG using inverse reinforcement learning and an improved alternating direction method of multipliers, the proposed method addresses a broader and more complex scenario. The strategy in [36] was designed for centralized scheduling within a single MG and did not consider coordination between multiple MGs or dynamic sharing of active power among them. Furthermore, [36] prioritized cost minimization and resilience to forecasting errors but did not incorporate conflicting environmental objectives into its formulation. Nor did it address system-level challenges such as dynamic coordination between different inverter types or the implications of real-time communication constraints.

Finally, there is a lack of detailed comparisons between different hierarchical control schemes, particularly regarding proportional energy sharing based on emission factors and total losses of the MGC, making it challenging to assess the relative effectiveness of the proposed methods.

The proposed control scheme aims to address these key challenges by integrating a multi-objective optimization framework within the hierarchical control architecture. This framework simultaneously minimizes operational costs and CO_2 emissions, thereby improving both economic and environmental performance. It incorporates an emission-aware energy distribution strategy among MGCs, ensuring that energy sharing decisions prioritize sustainability without compromising system cost. Moreover, the control method implements an enhanced droop control technique designed to reduce total network losses while maintaining simplicity and adaptability for practical deployment. To validate its effectiveness, the scheme has been tested in real-time simulation environments, demonstrating computational efficiency and robustness under dynamic operating conditions. Furthermore, by providing a comprehensive comparison with existing hierarchical controls—focusing on proportional-based power sharing—this work enables a clearer assessment of trade-offs and benefits, supporting informed decision-making in integrated MG control.

In light of the current limitations in research, this article presents the following contributions aimed at addressing the gaps identified in the existing literature:

- Design of an optimized hierarchical control for an IMGC based on GS and grid GF inverters in real-time, enabling the simultaneous optimization of costs and emissions through a multi-objective particle swarm optimization (MOPSO) algorithm within the hierarchical architecture. The tertiary control is responsible for distributing energy between the MG connected with a GF converter and the MGs connected with GSs converters, considering the CO_2 emissions associated with energy generation in each MG. The adaptive primary control optimizes the droop control coefficients while accounting for losses in transmission lines, filters, and power transformers to achieve optimal power dispatch in the MGs. Moreover, a centralized secondary control is considered to correct voltage and frequency variations produced in the primary control.
- Development of a system to quantify and minimize the losses of the MGC, demonstrating that it is possible to achieve this solely based on the droop control coefficients and the frequency values measured in the IMGC. This represents a simple and flexible method to be exported to another IMGC based on converters that apply the droop control technique, which is the most widely used technique in primary control.
- Real-time validation of the proposed control based on hardware-in-the-loop experimentation using an OPAL-RT4512 emulator and a dSPACE MicroLabBox controller. Simulations with dynamic loads were conducted in the MATLAB/Simulink environment and verified in real-time simulations, demonstrating the practical viability of the proposed control scheme and its computational effectiveness by being able to replicate in real time.
- Comparison of the proposed MOPSO hierarchical control with a hierarchical control based on proportional energy distribution according to the emission factors of each MG, which implements a primary control based on proportional distribution according to the rated powers of the converters, thus eliminating the need for a secondary control.

This paper is organized as follows: Section 2 describes the configuration of the IMGC based on GS and GF converters, along with their cascade control system. Section 3 introduces the MOPSO for optimized hierarchical control of the IMGC. Section 4 details the proportional hierarchical control for comparison with the control presented in Section 3. Section 5 presents the results and discussions from MATLAB/Simulink simulations and experimental tests conducted in a real-time HIL environment. Finally, Section 6 summarizes the conclusions derived from this study.

2. Configuration of the IMGC

In islanded applications, one or more converters must be a GS inverter. This is crucial for maintaining voltage and frequency stability, compensating for the lack of a central grid. Usually, droop control is implemented in these scenarios. Nevertheless, these converters do not

directly control active or reactive power based on a preset reference. Therefore, GF inverters are designed to inject a specific amount of power into the IGMC.

In this paper, the two aforementioned inverter typologies are optimally combined. Fig. 1 illustrates the configuration of the proposed IMGC. Three MGs comprise the IMGC, two of them connected to GS inverters and a third connected to a GF inverter. Each converter outputs an AC voltage level of 480 V. To enhance the quality of the output signal and achieve a more stable and controlled voltage, an RLC filter is included. Finally, a step-up transformer raises the voltage from 480 V to 600 V, along with a set of connection lines between the MGs and the common coupling point (PCC), where a set of dynamic loads are connected.

Fig. 2 depicts the cascade control scheme for the IMGC. To manage the operation of each MG, a local control strategy is implemented for each inverter, employing a cascade control approach. This method is frequently utilized in MG management because it enhances the precision of system control. By employing several controllers in a nested loop arrangement, straightforward linear control techniques can be applied, resulting in quicker response times and improved disturbance mitigation. In the proposed IMGC, the cascade control framework consists of four controllers arranged sequentially for the GS inverters, while three controllers comprise the GF inverter control. The output of each controller serving as the input for the subsequent one.

For the two MGs connected through GS converters, the local control is composed of an optimized droop control, a current controller, a voltage controller and an inverter gates generator. The first controller employed is the droop control, where the frequency of each MG can be defined as follows:

$$f_i = f_{o,i} + n_i\left(P_{o,i} - P_i\right) \tag{1}$$

In this context, f_i represents the frequency measured for each MG, while $f_{o,i}$ indicates the reference frequency. The droop control coefficient is denoted as n_i, $P_{o,i}$ signifies the power corresponding to the frequency $f_{o,i}$, and P_i is the active power that has been measured. It is essential to recognize that the subscript i refers to each individual MG.

Following a similar approach, the output voltage from each MG can be derived from the subsequent equation:

$$V_i = V_{o,i} - m_i Q_i \tag{2}$$

where V_i denotes the output voltage, $V_{o,i}$ represents the reference voltage, m_i is the coefficient for voltage droop control, and Q_i indicates the measured reactive power. It is important to mention that for the voltage droop control scenario, $Q_{o,i}$, is considered to be zero.

After determining the value of f_i, the phase, wt, is calculated. This term is essential for transforming the sinusoidal current and voltage measurements (I_{abc}, V_{abc}) into the direct-quadrature coordinate system, resulting in $V_d^*, V_q^*$and I_d^*, I_q^*. This transformation simplifies the application of PI controllers. The voltage control system is tasked with modifying the measured values of V_d, V_q to align with the desired targets obtained from Eq. (2). A PI controller is employed to minimize the discrepancy between the actual and target values, V_d, V_q and V_d^*, V_q^*. Consequently, the output from each PI controller provides the reference current values for the converters, denoted as I_d^*, I_q^*.

The current control loop is designed to align the measured values of I_d, I_q with the previously determined reference values. A PI controller is utilized to minimize the error between the actual currents and the reference currents, I_d, I_q compared to I_d^*, I_q^*. The output from these PI controllers is labelled as $v_{d,i}$ and $v_{q,i}$, representing the voltage values that each GS inverter must regulate. Since the 'd' and 'q' components are interdependent, decoupling of the axes is essential. This is accomplished through feedforward decoupling, which computes the control components of the converter as $V_{d,con}$, and $V_{q,con}$. The PWM block generates the triggering signals for the IGBTs of the GS inverter, enabling control over voltage and frequency in accordance with the optimized droop control strategy illustrated in Fig. 2.

For the MG connected through a GF inverter, the cascade control approach is modified. Initially, these converters must achieve precise synchronization with the AC voltage at the connection point. Usually, this is achieved by utilizing a synchronization algorithm such as a phase-locked loop (PLL) to accurately deliver active and reactive power. The PLL transforms the three-phase voltage waveforms from the reference frame into a rotating dq0 reference frame via the Park transformation.

Secondly, the droop control and the voltage controller are replaced by a power controller. In this context, the reference values of active and reactive power (P and Q) are divided by the measured values of V_d to generate the reference currents I_d^*, I_q^*, which are then utilized in the current control loop. The remainder of the cascaded control scheme is identical to that used for the GS inverter.

3. MOPSO hierarchical control

3.1. Hierarchical control scheme

This section describes the proposed MOPSO for the IMGC. Unlike other works, a control architecture is implemented in real time, which

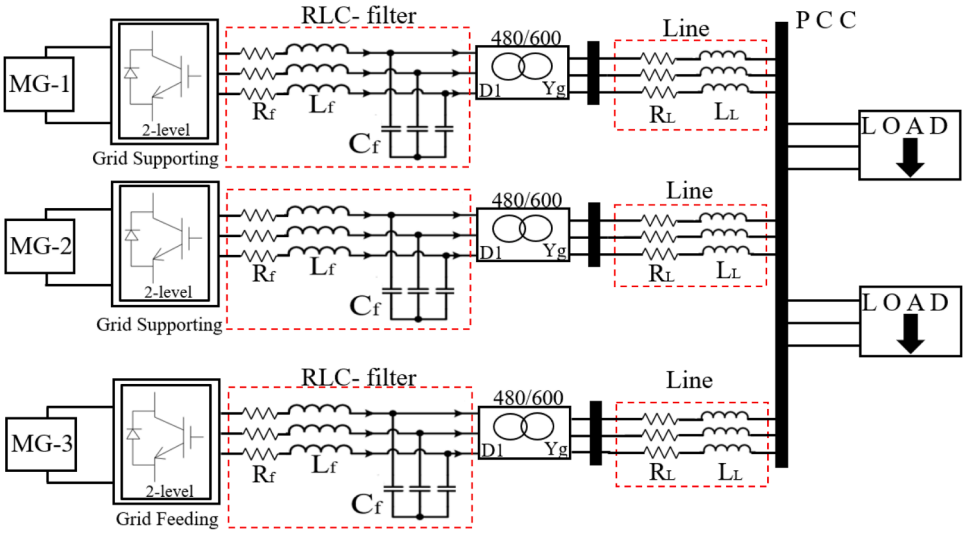

Fig. 1. Configuration of the IMGC under study.

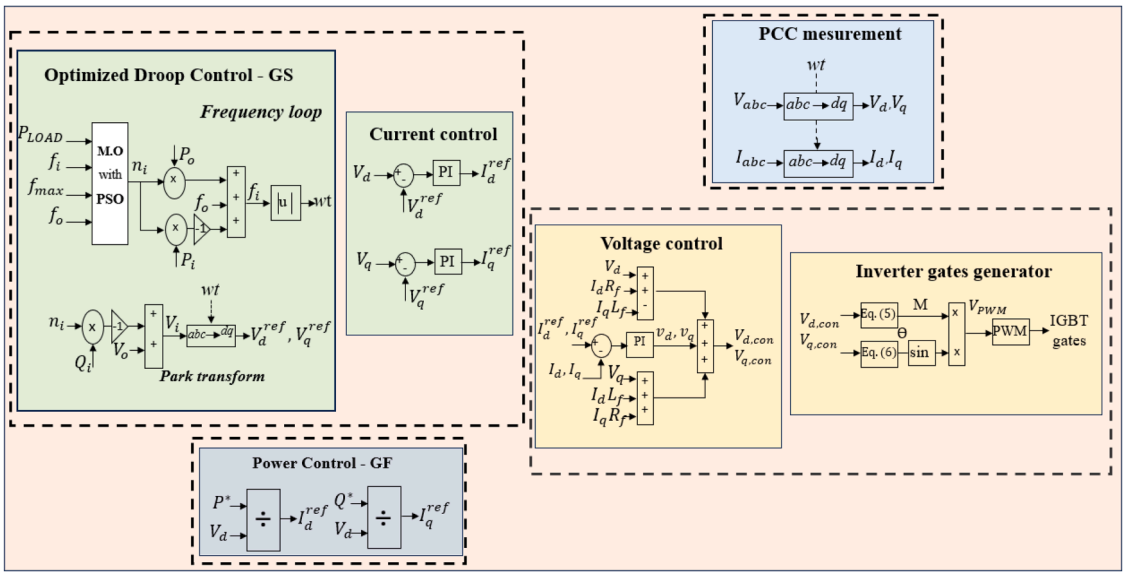

Fig. 2. IMGC local control scheme.

evaluates the distribution of energy among the MGs connected through GS inverters and the MG connected through the GF inverter, based on the CO_2 emissions associated with each MG. Furthermore, it presents how the droop control coefficients can be effectively adapted to achieve an optimal power dispatch that minimizes total losses.

Fig. 3 illustrates the optimized hierarchical control scheme based on MOPSO. Starting from a top-down structure, the tertiary control is responsible for distributing energy among the MGs. Since the power to be generated is directly controlled in the MG connected through a GF inverter, the power dispatch can be expressed as follows:

$$P_{LOAD} = P_{MG,1-2} + P_{MG,\ 3} \tag{3}$$

where P_{LOAD} refers to the total active power demand, $P_{MG,1-2}$ is the active power that must be generated by the MGs connected through GS inverters, and $P_{MG,\ 3}$ represents the active power that must be generated by the MG connected through the GF inverter.

To simplify the notation, subscripts 1 and 2 are used for the MGs connected with GS inverters, while subscript 3 denotes the MG connected through a GF inverter. Once the value of $P_{\ 3}$ has been obtained, the pulses of the GF inverter are generated as detailed in Section 2, in order to manage the power indicated by the tertiary control.

In the case of GS inverters, the remaining power needed to meet the demand is optimally controlled indirectly through the droop control coefficients at the primary control level. The MOPSO is responsible for generating the optimal values of the droop coefficients that minimize the cost function, as detailed in Section 3.2. The primary control responds quickly and in a decentralized manner to maintain the immediate stability of the IMGC. However, due to disturbances caused by variations in demand, the frequency and voltage values deviate from their nominal levels. This is why a centralized secondary control is implemented in this paper to re-adjust these deviations back to the rated values. Two independent PI controllers are responsible for adjusting the error between the measured values of frequency (f_{meas}) and voltage (V_{meas}), and the rated values of these parameters for the IMGC, f_{nom} and V_{nom}. The terms f_o and V_o refer to the adjustments made by the secondary control to ensure that the frequency and voltage of the IMGC remain at their nominal values. Once the values of f_i and V_i have been obtained, the cascaded voltage and current control loops generate the pulses for the GS inverters, thereby producing the necessary power to complete the

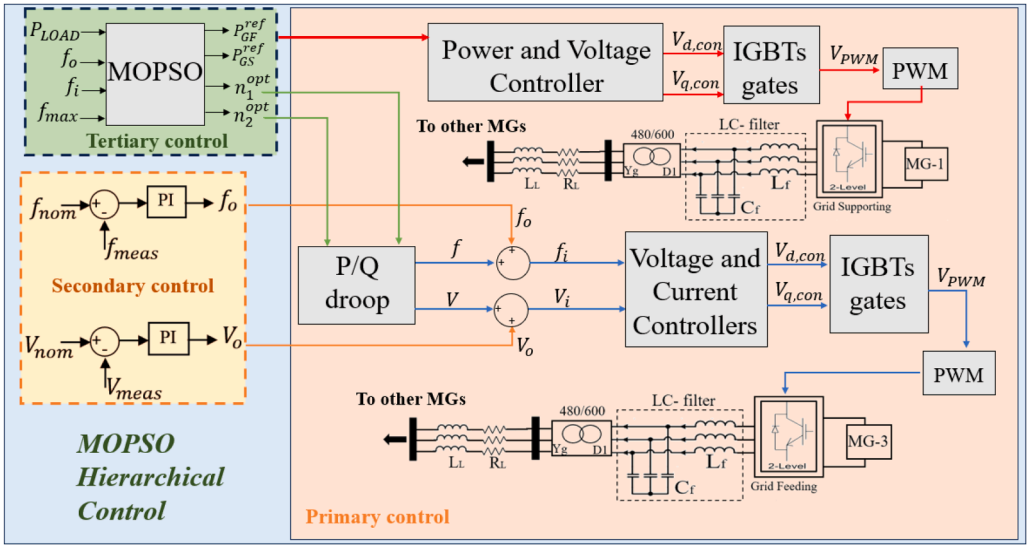

Fig. 3. MOPSO hierarchical control architecture.

power balance.

3.2. MOPSO optimization

This section outlines the formulation of the MOPSO to simultaneously optimize emissions and costs. The multi-objective function is expressed as:

$$M.O.F = \min\left(w_1 \cdot OF_1 + w_2 \cdot OF_2\right) \tag{4}$$

where OF_1 denotes the objective function employed to calculate the CO_2 emissions associated with the generation of MG, and OF_2 represents the function that expresses the operational costs of each MG. The weights w_1 and w_2 are used to consider each objective function within the multi-objective optimization. The emission optimization is used to allocate energy between MG_{1-2} and MG_3. Subsequently, the cost optimization is applied to adjust the droop control coefficients and reduce losses within the IMGC. This approach enables a reduction in operational costs by minimizing energy generation losses.

According with [37], CO_2 emissions can be expressed as a cubic function of the power delivered by each MG as:

$$OF_1 = \sum_{i=1}^{n} E_i \cdot \left(\mathrm{a} \cdot P_i^3 + b \cdot P_i^2 + \mathrm{c} \cdot P_i + \mathrm{d}\right) \tag{5}$$

where E_i is a factor that defines the CO_2 emissions for each MG, P_i refers to the generation of each MG, and *a, b, c*, and *d*, are constant values that define the equivalent CO_2 emissions for the DERs of each MG. These values are obtained from [38,39].

Since the main objective of this function is to allocate energy among the MGs, two constraints must be satisfied simultaneously. First, Eq. (3) must be fulfilled to ensure demand is met. Moreover, the power of the MGs is constrained between 0 and the inverter's rated power to ensure operation under safe nominal conditions. MG_1 has a rated power of 500 kW, MG_2 presents a rated power of 250 kW and MG_3 has a rated power of 300 kW.

The function OF_2 denotes the operational costs of the MGs that operate with GS inverters. This article proposes an approach that allows for the optimization of the total losses in the IMGC, not just the losses in the transmission lines, as previous works [40]. To achieve this, this work demonstrates that solely adapting the droop coefficients allows for maintaining voltage and frequency values within the established thresholds.

Eq. (6) shows the operating cost objective function:

$$OF_2 = \sum_{i=1}^{n} C_i P_i + C_{LOS,i} P_{LOS,i} \tag{6}$$

where C_i represents the MG operating cost, C_{LOS} refers to the expenses associated with the losses, and P_{LOS} accounts for the total losses within the IMGC. These losses include those occurring in the lines, filters, and transformers.

As indicated by Eq. (1), the MG output power depends on the frequency and droop coefficients. Therefore, the term $P_{o,i}$ can be written as:

$$P_{o,i} = P_{f,max} + \frac{f_{max} - f_{nom}}{n_i} \tag{7}$$

where $P_{f,max}$ is the power at the highest frequency, and f_{max} is the highest allowable frequency.

By assigning a value of 0 to $P_{f,max}$ and setting $f_{nom} = 1$ pu, P_i can be derived using Eqs. (1) and (7) as:

$$P_i = \frac{f_{max} - 1 + f_{o,i} - f_i}{n_i} \tag{8}$$

The losses $\left(P_{LOS,i}\right)$ are given as follows:

$$P_{LOS,i} = 3I_i^2 R_i \quad I_i = \frac{P_i}{\sqrt{3} V_i cos_{\varphi i}} \tag{9}$$

where I_i represents the current flowing through each MG, $R_i$indicates the total losses and $cos_{\varphi i}$ denotes the power factor.

By integrating Eqs. (7)-(9), Eq. (6) can be formulated in terms of f and n_i. Particularizing for the case study in this paper, it can be expressed as:

$$\begin{aligned} OF_2 = {} & C_1\left(\frac{f_{max} - 1 + f_{o,1} - f_1}{n_1}\right) + C_2\left(\frac{f_{max} - 1 + f_{o,2} - f_2}{n_2}\right) \\ & + C_{LOS,1}\left(3\left(\left(\frac{f_{max} - 1 + f_{o,1} - f_1}{n_1 \sqrt{3} V_1 cos_{\varphi 1}}\right)^2\right) R_1\right) \\ & + C_{LOS,2}\left(3\left(\left(\frac{f_{max} - 1 + f_{o,2} - f_2}{n_2 \sqrt{3} V_2 cos_{\varphi 2}}\right)^2\right) R_2\right) \end{aligned} \tag{10}$$

Moreover, the constraints that must be met to adequately satisfy the OF_2 are expressed as follows:

$$n_i \in [lb, ub] P_1 + P_2 = P_{MG,1-2} + P_{LOS,1} + P_{LOS,2} \tag{11}$$

where lb, ub denote the lower and upper thresholds for the droop coefficients.

Moreover, the power balance must be maintained, where MG_1 and MG_2 must supply the power assigned by the tertiary control, considering the total system losses. By adapting the droop coefficients in real-time, it is possible to indirectly control the power of the GS inverters.

As a result, the objective function for operational costs depends exclusively on the droop control coefficients and frequency. By effectively adapting these coefficients, it is possible to significantly minimize energy losses, as represented by the third and fourth summands of Eq. (10), leading to a reduction in operational expenses. This approach enables loss optimization in a IMGC by knowing the resistance values, the thresholds at which frequency control is desired, and the unit operating costs of each MG. These are general measurements that are accessible in any MGC, making the proposed method a flexible and easily reproducible approach for losses optimization studies.

One of the main strengths of the proposed approach lies in its inherent scalability to larger IMGCs. This is enabled by the general structure of both the objective function (Eq. (10)) and the constraints (Eq. (11)), which were designed to be modular and easily extendable. Specifically, integrating additional MGs into the cluster results in new terms in the total equivalent emissions Eq. (5) and equivalent resistance (which denotes the total losses), as well as additional droop control coefficients in Eq. (10). This structure allows the optimization framework to expand proportionally with the number of MGs, without requiring fundamental reformulation. Importantly, the objective function is based on global indicators such as voltage and frequency deviations, which remain valid and effective even as the system scales. Because operational costs and power losses are strongly linked to each MG's droop coefficient, the control strategy maintains its performance and interpretability as the system grows. Therefore, the proposed method ensures computational feasibility and optimization consistency when applied to more complex IMGCs.

In this paper, the particle swarm optimization (PSO) algorithm is employed to solve the previously described optimization problem. The PSO algorithm offers various advantages that distinguish it in the field of optimization methods. Unlike other algorithms, PSO does not depend on the derivatives of the objective function, such as the gradient method [41], or Lagrange optimization [12], which makes it an effective algorithm for tackling nonlinear or discontinuous problems.

Furthermore, the population-based characteristic of PSO allows for a thorough exploration of the solution space, thus minimizing the risk of converging to local minima [42]. Another significant advantage of PSO is its ability to achieve rapid convergence to optimal solutions, which is

particularly valuable when addressing high-dimensional problems.

PSO algorithm is a metaheuristic algorithm based on the collective behaviour of a group of particles that explore the solution space. Each particle adjusts its position based on its own experience and that of its neighbours, seeking the best solution according to a fitness criterion. The position of each particle at any given time is given by:

$$x\ (k+1) = x(k) + v(k+1) \tag{12}$$

where x denotes the position of each particle at an instant k, and v denotes the velocity of each particle.

$$v(k+1) = w \cdot v^k \ + \ r_1 c_1 \left({x_{pbest}}^k - x^k \right) \ + r_2 c_2 \left({g_{pbest}}^k - x^k \right) \tag{13}$$

The inertia factor is defined as w. Moreover, r_i represents stochastic random coefficients that range between 0 and 1, c_1 denotes the cognitive acceleration coefficient, c_2 illustrates the social acceleration coefficient, x_{pbest} indicates the best position achieved by the particle up to the current iteration and x_{pbest} is the global best position. It is important to note that the superscript k refers to the current iteration:

$$w(k) = \frac{w_{max} - w_{min}}{n_{iter}} \tag{14}$$

where w_{max} is the maximum inertia factor, w_{min} is the minimum inertia factor, and n_{iter} is the number of iterations.

The MOPSO algorithm implemented in this work incorporates a dynamic balance between exploration and exploitation through the adaptive adjustment of the inertia weight parameter during the optimization process. At early iterations, a higher inertia weight promotes extensive exploration of the solution space, enabling the swarm to avoid premature convergence on suboptimal local minima by broadly sampling diverse regions. As the search progresses, the inertia weight is gradually decreased to enhance exploitation capabilities, allowing particles to intensify the search around promising areas identified during exploration.

This inertia weight scheduling is critical in mitigating the risk of stagnation in local minima, as it prevents particles from becoming trapped too early in limited regions of the search space. Furthermore, the collective social and cognitive components of the particle velocity update ensure that particles are simultaneously influenced by both their individual historical best solutions and the global best solution found by the swarm. This fosters diverse search trajectories and preventing convergence to isolated local optima. Hence, the combination of adaptive inertia weighting and the dual social-cognitive guidance mechanisms within the MOPSO framework enhances the algorithm's ability to effectively navigate complex, multimodal solution spaces, reducing the likelihood of convergence to local minima and improving the robustness and quality of the optimal solutions

The MOPSO algorithm applied in this work was configured with parameter values adapted from commonly accepted ranges in the literature. This ensures robust convergence and a balance between exploration and exploitation. Table 1 summarizes the main parameters. Specifically, the inertia weight was linearly decreased from an initial value of w_{max}= 0.896 to a final value of w_{min}= 0.800. This gradual shift moves the swarm behavior from exploration to exploitation. The cognitive and social acceleration coefficients were set to c_1=0.95 and c_2 =0.85, respectively, to maintain a stable balance between individual and collective learning during the search process.

Table 1
MOPSO parameters.

Symbol	Parameter	Value
w_{max}	Maximum inertia weight	0.896
w_{min}	Minimum inertia weight	0.8
c_1	Cognitive acceleration coefficient	0.95
c_2	Social acceleration coefficient	0.85
n_p	Number of particles	30
n_{iter}	Number of iterations	150

These parameter values aling with the recommendations reported by [43], whose study on multi-objective PSO demonstrated stable convergence behavior and effective solution diversity in complex engineering problems. In this work, the number of particles and the number of iterations were set to 30 and 150, respectively. This selection ensures a trade-off between exploration capacity and computational speed. These values were selected specifically to meet the real-time constraints imposed of the control architecture, which operates with a very short sampling interval of 50 micro-seconds. Therefore, the algorithm must reach a satisfactory solution within computational feasibility [44].

One of the key challenges in multi-objective optimization design is the appropriate selection of weighting factors for each control objective. In this work, a graphical approach was used to support the weight selection, as shown in Fig. 4. Fig. 4a depicts how OF_1, representing emissions, evolves with respect to the weights w_1 and w_2. Simultaneously Fig. 4b represents the variation of OF_2, illustrating power losses, under the same weighting combinations. Moreover, Fig. 4 includes all possible combinations of w_1 and w_2 that satisfy the constraint $w_1 + w_2 = 1$, thereby ensuring that both objectives are considered concurrently.

From the plot in Fig. 4a, it can be observed that when $w_1 = 1$ and $w_2 = 0$, the optimization focuses entirely on minimizing emissions, leading to the lowest possible value of OF_1. As w_1 decreases and w_2 increases, the influence of emissions on the optimization gradually reduces in favor of minimizing losses. For instance, at $w_1 = 0$ and $w_2 = 1$, the optimization is fully oriented towards reducing OF_2, achieving its lowest possible value.

Similarly, Fig. 4b illustrates the inverse behavior for OF_2. When $w_2 = 1$, losses are minimized. As w_2 decreases and w_1 increases, losses become less prioritized, resulting in higher OF_2 values while emissions are progressively minimized. This symmetrical behavior across both figures clearly highlights the trade-off between the two objectives as a function of the assigned weights.

This analysis offers compelling evidence of how variation in w_1 and w_2 directly affects the outcome of the multi-objective optimization. Therefore, to achieve a fair compromise without favoring one objective over the other, and based on the graphical sensitivity study performed, equal weighting factors of $w_1 = 0.5$ and $w_2 = 0.5$ were adopted. This balanced choice ensures that both objectives are simultaneously optimized, leading to a well-balanced solution where neither function is prioritized.

Beyond the sensitivity analysis of selected weighting factors, it is essential in multi-objective optimization to explicitly depict the Pareto-optimal front. This reveals the inherent trade-offs between the conflicting objectives of CO_2 emissions and power losses. Accordingly, a systematic sweep of the objective function weights w1 and w2, constrained by w1+w2=1, was performed to generate the Pareto front presented in Fig. 5. In Fig. 5, the X-axis represents the calculated CO_2 emissions function, while the Y-axis corresponds to the associated power losses function for each evaluated weight combination.

Each point on the curve represents a distinct solution, obtained by prioritizing emissions or losses to a different extent. The resulting trend confirms the Pareto-optimal nature of the solutions: any improvement in one objective—such as reducing losses—leads unavoidably to a deterioration in the other—such as increased emissions. For example, shifting from weights (0.3,0.7) to (0.2,0.8) reduces the losses objective at the cost of higher emissions, clearly illustrating the necessary compromise between criteria. The concave shape and monotonic behavior of the curve in Fig. 5 provide clear empirical evidence of this trade-off, validating that the set of solutions lies on the Pareto front. This graphical representation enhances the decision-making process, allowing for the selection of operating points aligned with specific regulatory, environmental, or operational priorities.

Furthermore, to empirically assess the complexity of the proposed MOPSO-based optimization strategy, a comprehensive scalability analysis has been conducted by progressively increasing the number of MGs

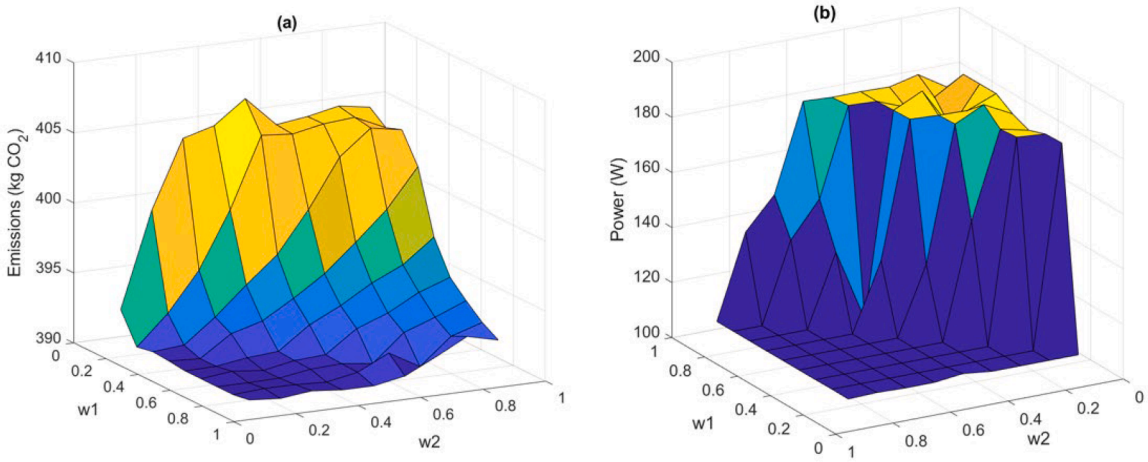

Fig. 4. Sensitivity analysis of MOPSO weighting factors: (a) Emissions as a function of w_1 and w_2, and (b) Power losses as a function of w_1 and w_2.

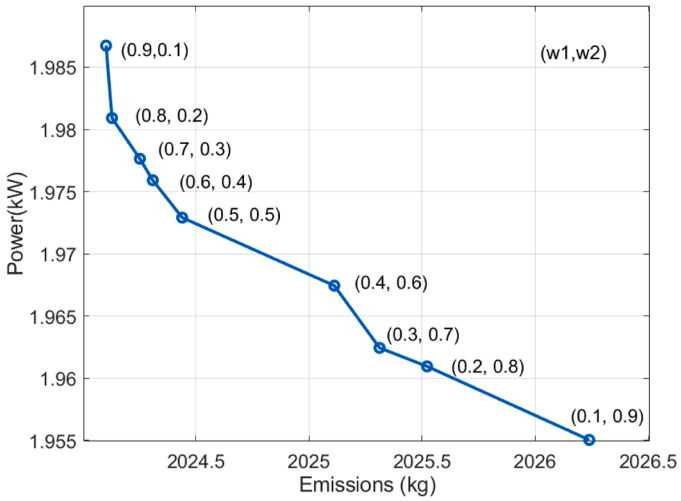

Fig. 5. Pareto-optimal solution between CO_2 emissions and power losses.

(n) in the MGC, from the baseline case of n=3 MGs (as proposed in this work) up to n=10 MGs. For each configuration, the number of iterations required to achieve convergence of the multi-objective function was recorded. The results are presented in Fig. 6, where each subfigure corresponds to a different MGC size.

In the case of 3 MGs (Fig. 6a), the optimization algorithm converges within 20 iterations. As the number of MGs increases, a consistent rise in the number of iterations is observed: for 4 MGs (Fig. 6b), convergence is achieved in 26 iterations; for 6 MGs (Fig. 6d), 57 iterations are required; and for 9 MGs (Fig. 6g), the process takes 71 iterations. The most computationally intensive scenario analyzed, with 10 MGs (Fig. 6h), requires up to 100 iterations to reach convergence.

This behavior is a direct result of the increasing dimensionality and complexity of the optimization problem. As more MGs are integrated into the MGC, the number of decision variables—primarily the droop control coefficients for each MG—increases linearly. Simultaneously, the optimization must satisfy a growing set of power balance constraints and ensure coordination among MGs that meets both global objectives (e.g., emissions minimization, power loss reduction) and local operational constraints. This significantly expands the search space, thereby increasing the computational effort required by the MOPSO algorithm to adequately explore the optimal solution.

Moreover, the presence of conflicting objectives in high-dimensional systems amplifies the difficulty of finding well-balanced multi-objective solutions, especially as interactions between MGs becomes more coupled. Consequently, both the number of iterations and the computation time per iteration increase, reflecting the empirical complexity introduced by larger MGC configurations.

4. Proportional hierarchical control benchmark

In this section, a hierarchical control based on a proportional power allocation approach is presented, serving as a benchmark to compare with the hierarchical control based on MOPSO proposed in this paper. The proportional tertiary control is based on allocation factors that consider the emissions of each MG. These factors are used to determine an initial distribution of the total power (P_{TOTAL}) proportionally to the inverse of the emissions:

$$\alpha = \frac{E_3}{E_{1-2} + E_3} \quad \beta = \frac{E_{1-2}}{E_{1-2} + E_3} \tag{15}$$

where α represents the allocation factor associated with MG_{1-2} and β is the allocation factor associated with MG_3.

Once the allocation factors have been calculated, the power is assigned to each MG according to:

$$P_{MG,1-2} = P_{TOTAL} \cdot \alpha \; P_{MG,3} = P_{TOTAL} \cdot \beta \tag{16}$$

To ensure proper operation, a minimum operating limit of each MG is set at 10% of its nominal power to meet the demand. The allocation ensures that the rated operating limits of each inverter are not exceeded.

Secondly, a droop control based on proportional allocation is adapted. This approach eliminates the need for a supervisory secondary control. The proportional allocation-based on droop control relies on adjusting the droop coefficients according to the nominal power of the converters, ensuring that they always operate at the operating point defined as (f_o, P_o).

The power received by each MG is distributed according to:

$$P_{o,1} = P_1 = P_{MG,1-2} \cdot \frac{1}{\left(1 - \frac{P_2^{rated}}{P_1^{rated}}\right)} \quad P_{o,2} = P_2 = P_{MG,1-2} \cdot \frac{1}{\left(1 - \frac{P_1^{rated}}{P_2^{rated}}\right)} \tag{17}$$

The power to be delivered by each MG connected to a GS inverter is controlled to match the power P_o. To this end, the droop control coefficient can be determined from the following expression:

$$n_i = \frac{f_{max} - f_{o,i}}{P_{o,i}} \tag{18}$$

By grouping Eq. (18) into Eq. (1), the following expression is obtained:

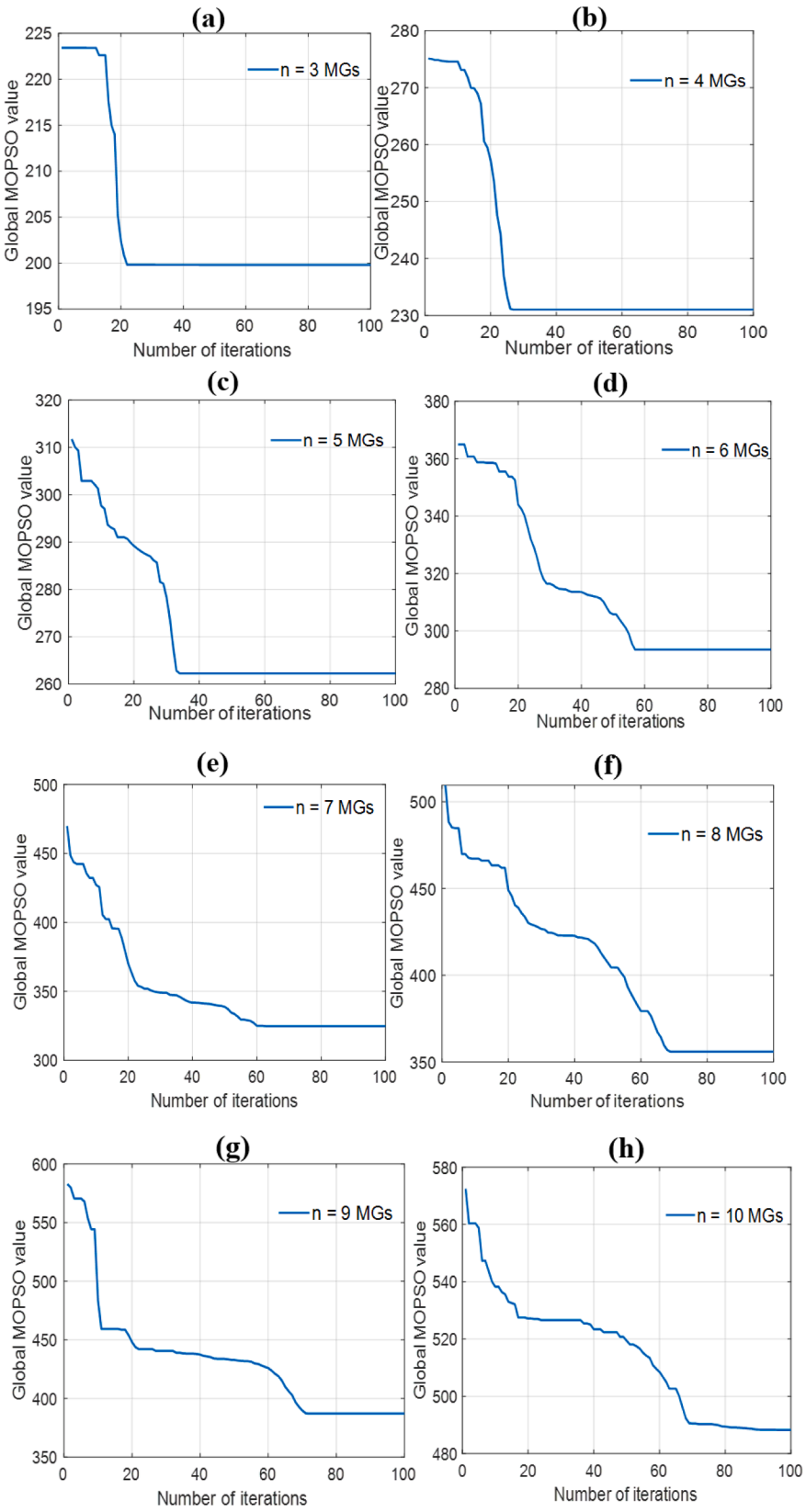

Fig. 6. MOPSO convergence against MGs counts: (a) 3 MGs, (b) 4 MGs, (c) 5 MGs, (d) 6 MGs, (e) 7 MGs, (f) 8 MGs, (g) 9 MGs and (h) 10 MGs.

$$f_i = f_{o,i} + \frac{f_{max} - f_{o,i}}{P_{o,i}}\left(P_{o,i} - P_i\right) = f_{o,i} \tag{19}$$

The designed proportional droop control demonstrates that by adjusting the value of n_i according to Eq. (18), it is possible to establish an operation such that the output frequency f_i=$f_{o,i}$. This implies that the droop control adjusts proportionally to variations in the power managed by the converter, ensuring that it operates at $f_{o,i}$ under any condition.

Therefore, the need to implement a secondary control to restore the values of f_i is avoided.

5. Results and discussion

5.1. MOPSO general performance

This section presents the results of MOPSO-based hierarchical control in different scenarios. First, Section 5.1 outlines the general operation of MOPSO under dynamic variations of active and reactive power. Section 5.2 compares the results of the proposed hierarchical control with the hierarchical benchmark control introduced in Section 4. Section 5.3 examines the system operation under fault conditions, demonstrating the stability of the system when one MGs is disconnected from the IMGC. Finally, to validate the practical feasibility of the proposed approach, Section 5.4 presents real-time HIL tests, which corroborate the results obtained from MATLAB/Simulink simulations. To assess the computational performance of the proposed MOPSO algorithm, all simulations were conducted using MATLAB/Simulink R2022a. The simulations ran on a desktop computer featuring an AMD Ryzen 7 7700 × 8-core processor (4.50 GHz), 64.0 GB of RAM, and Windows 11 Enterprise. A discrete solver with a fixed time step of 50 micro-seconds was employed. Under these conditions, simulating an 1800-second scenario took 30 minutes, demonstrating the computational efficiency of the proposed approach. This level of computational feasibility also validates the suitability of the proposed MOPSO scheme for real-time applications, as was evidenced by the HIL implementation in OPAL-RT4512 and dSPACE MicroLabBox. The figures are presented on a time scale in seconds, with 300 s intervals, to appropriately represent the different operating scenarios.

A simulation time step of 50 μs was employed across all scenarios to ensure an accurate representation of the IMGC's fast dynamic behavior. In this context, both the controller execution and the runtime of the embedded optimization algorithm were completed within the same 50 μs step on the HIL platform, ensuring true real-time operation of the entire control loop. This resolution is necessary to properly capture the high-frequency switching of the inverters, their modulation strategies, and the rapid transients involved in power sharing and IMGC dynamics [45]. In particular, the selected time step allows the model to reflect the instantaneous effects of the droop-based control and the response of the GS and GF inverters under varying load and generation conditions. Moreover, maintaining a uniform step size across all simulation stages—including normal operation and fault-mode scenarios—ensures numerical stability and consistency, which are essential for both offline analysis and real-time HIL validation.

Fig. 7 shows a simulation of 1800 s, considering multiple dynamic variations of the active and reactive power demanded. Fig. 7a illustrates the values of active (P_{PCC}) and reactive (Q_{PCC}) power measured at the PCC. P_{PCC} varies between 250 and 800 kW, while Q_{PCC} is between 0 and 100 kVAr. Fig. 7b and Fig. 7c depict the frequency and voltage of the IMGC measured at the PCC. The IMGC parameters are presented in Table 2.

It can be seen that when the load is kept constant, the frequency remains stable at 60 Hz and the voltage at 600 V. As the active power demand increases at 300 s, from 374 kW to 574 kW, both the frequency and voltage exhibit minor oscillations but quickly stabilize, demonstrating effective control under the system disturbance. Similarly, a sharp decrease in the demand at 700 s, from 780 kW to 475 kW, results in stable frequency. At 800 s, Q_{PCC} rises to 90 kVAr, and decreases to 30 kVAr at 1140 s, while frequency and voltage remain stable.

A more challenging disturbance for the IMGC occurs at 1500s, when the demand abruptly decreases from 575 kW to 224 kW. This sudden reduction in demand causes a transient increase in both frequency and voltage. As shown in Fig. 5b and Fig. 5c, the maximum frequency and voltage reach 60.14 Hz, and 616.7 V, respectively. These values remain

Table 2
IMGC parameters.

Symbol	Parameter	Unit	Symbol	Parameter	Unit
V_{nom}	Rated voltage	600 V	n_p	PSO number of particles	30
f_{nom}	Rated frequency	60 Hz	n_{iter}	PSO number of iterations	150
L_f, R_f	Filter parameters	1.08 mΩ + 1.08 mH	l_b, u_b	Droop coefficients thresholds	[0.01, 0.08]
C	Filter capacitance	184 μF	f_{min}, f_{max}	Frequency range	[59.7, 60.3] Hz
Z_{LINE}	Transmission line parameters	5 mΩ +1 mH	V_{min}, V_{max}	Voltage range	[576, 624] V

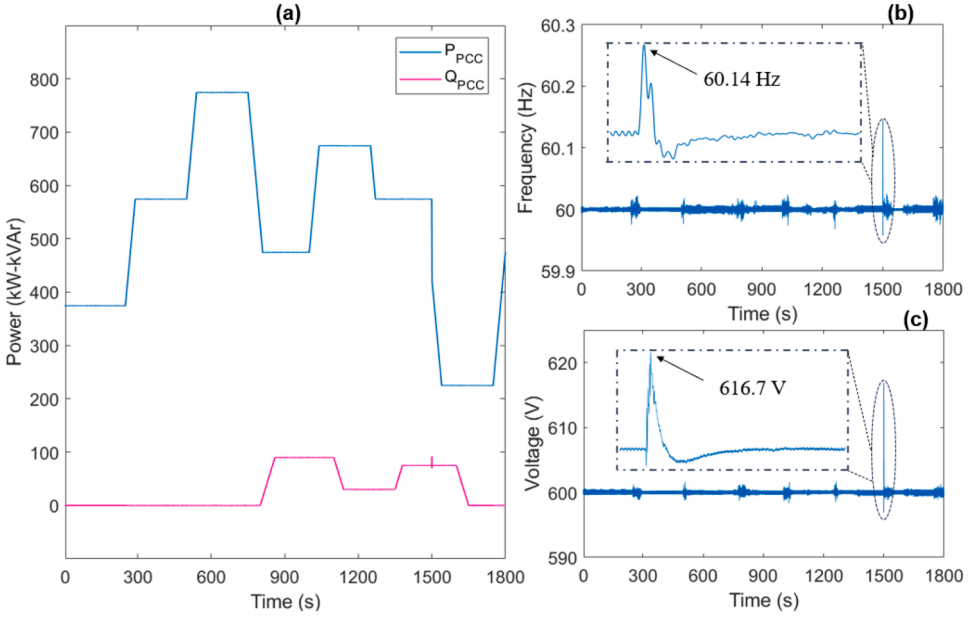

Fig. 7. IMGC measurements: (a) Active power (P_{PCC}), reactive power (Q_{PCC}), (b) IGMC frequency and (c) IGMC voltage.

within the specified limits of 60.3 Hz and 624 V.

Fig. 8a illustrates the active power distribution between MG_{1-2} ($P_{MG,1-2}$) and MG_3 ($P_{MG,3}$) to minimize CO2 emissions while meeting the demand. Fig. 8b shows the optimal droop coefficients for MG_1 ($n_{1,opt}$) and for MG_2 ($n_{2,opt}$). Fig. 8c and Fig. 8d depict the active (P_i) and reactive (Q_i) powers of each MG, respectively. Throughout the simulation, it can be seen that the power sharing between the MGs is done in such a way that $P_{MG,1-2} > P_{MG,3}$. This is primarily due to the higher maximum capacity of $P_{MG,1-2}$ (750 kW) compared to the maximum capacity of $P_{MG,3}$ (300 kW), which is necessary to meet the total demand. Moreover, the emissions associated with each MG play a crucial role in optimally allocating how energy should be distributed to meet demand and minimise emissions.

For instance, at the beginning of the simulation (up to 300 s), when $P_{PCC} = 374$ kW, the power distribution is $P_{MG,1-2}$=214 kW and $P_{MG,3} = 160$ kW. Similarly, around 1500s, with $P_{PCC} = 224$ kW, the distribution becomes $P_{MG,1-2} = 128$ kW, and $P_{MG,3} = 96$kW, proving that the demand is adequately met. In the first scenario, where $P_{MG,1-2} = 214$ kW, MOPSO assigns the optimal droop control coefficients of $n_{1,opt} = 4.5$ % and $n_{2,opt} = 4.9$ %. Therefore, $P_1 = 113$ kW and P_2 =101 kW.

For the second scenario, with $P_{MG,1-2} = 128$ kW, the assigned droop control coefficients are $n_{1,opt} = 7.5$ % and $n_{2,opt} = 8$ %, resulting in $P_1 = 66$ kW and $P_2 = 62$ kW. The power allocation is found to be adequate to meet the demand. As further demonstrated in Section 5.2, this allocation is optimal in terms of reducing CO_2 emissions and total losses within the IMGC. Regarding reactive power sharing, Q_3 is maintained at 0 kVAr throughout the simulation. The reactive power demand starts at 800s. Previously, Q_1 and Q_2 are adjusted to satisfy the reactive power consumption of the transmission lines between MGs, filters and transformers.

Fig. 9a and Fig. 9b depict the results of the optimal CO_2 emissions and total losses of the IMGC, respectively. The average values of emissions (E^{opt}_{avg}) and losses (P^{opt}_{avg}) are found to be 8.29 tons of CO_2 and 1.47 kW, respectively.

Finally, to quantitatively evaluate the stability margins of the proposed MOPSO-based control strategy, a detailed convergence analysis under varying load conditions and failure scenarios are presented in Table 3. To this end, ramp load variations are incorporated into the power dispatch scenario analyzed in Fig. 7, using a ramp rate of 50 seconds. This assessment considers fluctuations in power demand ranging from 225 kW to 774 kW, encompassing a representative spectrum from low to high-load scenarios. Moreover, the failure scenario is based on the sudden disconnection of one MG (as further discussed in section 5.3). This analysis includes abrupt demand changes, which pose a more challenging problem for control stability. The stability evaluation was conducted by calculating critical frequency regulation parameters, including overshoot, settling time, and standard performance indices such as mean relative error (MRE), integral time absolute error (ITAE), integral time squared error (ITSE), integral absolute error (IAE), and integral squared error (ISE) during the transient response to load disturbances.

The results highlight a fast dynamic response, with an average settling time of 25.3 seconds. The maximum observed overshoot was limited to 60.16 Hz, while the minimum remained above 59.98 Hz, confirming the controller's ability to maintain frequency deviations within a narrow and safe band even under abrupt load changes. Moreover, the performance indices further validate the controller's effectiveness: the mean MRE was as low as $4.51 \cdot 10^{-9}$, the average ITAE was 53.78, the mean ITSE reached $3.46 \cdot 10^{-1}$, while the IAE and ISE averaged $5.79 \cdot 10^{-2}$ and $1.88 \cdot 10^{-3}$, respectively. Regarding the failure scenario, the metrics evidenced a maximum overshoot of 59.79 Hz, with a minimum settling time of 0.361 s, 1.21·10-6 MRE, 0.228 ITAE, $2.29 \cdot 10^{-2}$ ITSE, $1.51 \cdot 10^{-2}$ IAE and 1.51 · 10-3 ISE. These values collectively demonstrate that the MOPSO-based controller exhibits minimal error and excellent transient behavior. The combination of fast convergence, bounded overshoot, and low error metrics provides strong evidence that the proposed optimization-based controller is not only stable but also highly robust across a wide range of operating conditions.

5.2. Hierarchical proportional control

This section compares the results of the MOPSO with a proportional hierarchical control based on the emission factors of each MG and the nominal powers of their converters.

Fig. 10a shows the results for the proportional hierarchical control. A 30 s scenario is considered, with time intervals of 5 s. In the first scenario, $P_{MG,1-2} = 236$ kW, and $P_{MG,3}$=138 kW, satisfying the demand of

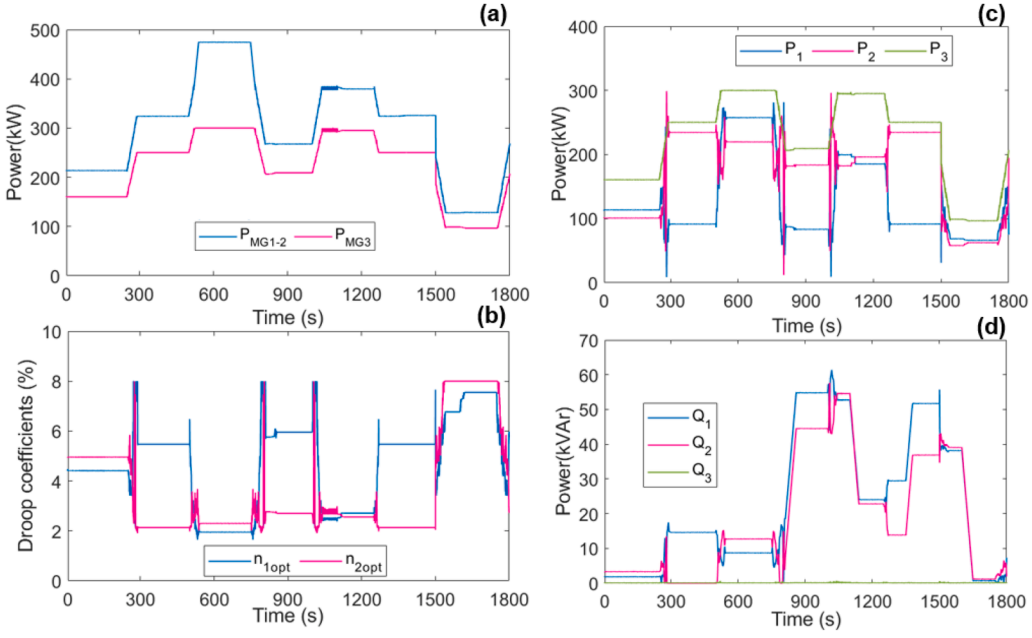

Fig. 8. MGs measurements: (a) Power distribution between MG_{1-2} ($P_{MG,1-2}$) and MG_3 ($P_{MG,3}$), (b) droop control optimal coefficients, (c) MGs active power (P_i), and (d) MGs reactive power (Q_i).

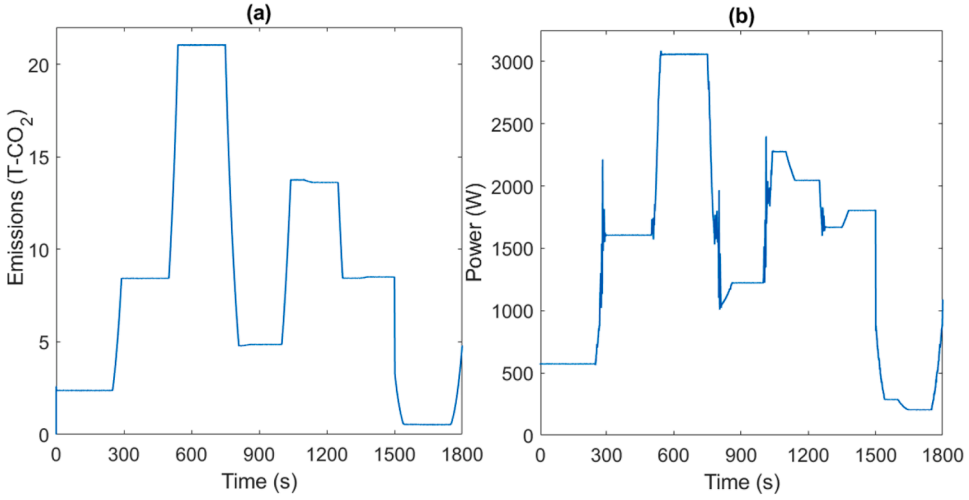

Fig. 9. Objective functions for MOPSO hierarchical control: (a) CO_2 emissions, (b) power losses.

Table 3
MOPSO control rate of convergence post-disturbance.

Time (s) - Scenario	Load (kW)	Frequency overshoot (Hz)	Settling time	MRE	ITAE	ITSE	IAE	ISE
[250,280.04]	[374-574]	59.98	30.04	$1.24{\cdot}10^{-8}$	16.11	$6.31\ 10^{-2}$	$6.07 \cdot 10^{-2}$	$2.37 \cdot 10^{-4}$
[500,520.6]	[574-774]	59.96	20.6	$5.27{\cdot}10^{-9}$	20.13	$7.14 \cdot 10^{-2}$	$3.95 \cdot 10^{-2}$	$1.40 \cdot 10^{-4}$
[750,779]	[774-474]	60,017	29	$1.40{\cdot}10^{-8}$	44.38	$1.43 \cdot 10^{-1}$	$5.81 \cdot 10^{-2}$	$1.87 \cdot 10^{-4}$
[1000,1029.7]	[474-674]	59.975	29.7	$8.66{\cdot}10^{-9}$	75.02	$3.33 \cdot 10^{-1}$	$7.40 \cdot 10^{-2}$	$3.29 \cdot 10^{-4}$
[1250,1262.5]	[674-574]	59.974	12,5	$2.38{\cdot}10^{-9}$	33.19	$1.28 \cdot 10^{-1}$	$2.64 \cdot 10^{-2}$	$1.03 \cdot 10^{-4}$
[1500,1530]	[575-225]	60.16	30	$1.61{\cdot}10^{-9}$	133.9	1.34	$8.85 \cdot 10^{-2}$	$8.89 \cdot 10^{-4}$
Fault sccenario	375 kW	59.79	0.361	$1.21{\cdot}10^{-6}$	0.228	$2.29 \cdot 10^{-2}$	$1.51 \cdot 10^{-2}$	$1.51 \cdot 10^{-3}$

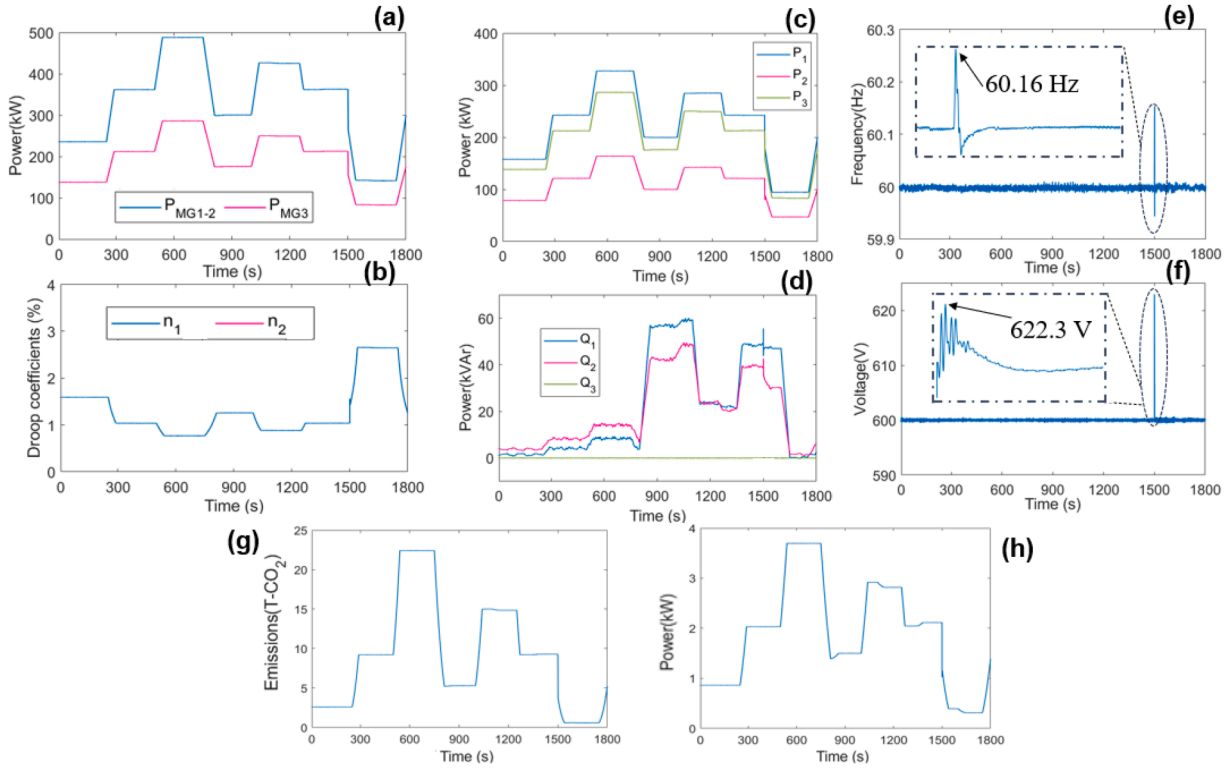

Fig. 10. Proportional hierarchical control results: (a). Power distribution between MG_{1-2} ($P_{MG,1-2}$) and MG_3 ($P_{MG,3}$), (b) droop control optimal coefficients, (c) MGs active power (P_i), and (d) MGs reactive power (Q_i), (e) frequency at PCC, (f) voltage at PCC, (g) CO_2 emissions and (h) power losses.

374 kW. In the second scenario, around 1500s, $P_{MG,1-2}$=141 kW and $P_{MG,3}$=83 kW, totalling 224 kW. Fig. 10b illustrates the droop control coefficients for proportional power sharing. In this approach, to maintain the IMGC frequency at f_i=60 Hz, n_1 and n_2 are set equal, ensuring proportional power variations for each MG in response to changes in the droop coefficients. Consequently, for $P_{MG,1-2}$ = 236 kW, the droop control coefficients are set to n_1 = 1.5 % and n_2 = 1.5 %, resulting in P_1 = 157 kW and P_2 = 79 kW, as shown in Fig. 10c. Despite identical droop coefficients, the power delivered by each one differs due to their different rated capacities. In the second scenario, with the droop control coefficients set to n_1= 2.6 % and n_2 = 2.6 %, the power values are P_1 = 94 kW and P_2 = 47 kW. Fig. 10d illustrates the reactive power values, where Q_3 is maintained at 0 kVAr and effectively responds to demand variations.

Fig. 10e and Fig. 10f represent the frequency and voltage values for the proportional hierarchical control, which are effectively controlled at 60 Hz and 600 V, respectively. Notably, this configuration does not employ a secondary supervisory frequency control. Nevertheless, the control strategy demonstrates an adequate response to abrupt demand variations at 1500s, with a maximum frequency of 60.16 Hz, and a maximum voltage of 622.3 V. Both values remain within the limits specified in Table 2.

Fig. 10g and Fig. 10h depict the emission and power losses values for this configuration. The average emission value (E_{avg}) is 8.92 tons of CO2, and the average loss value (P_{avg}) is 1.87 kW. These results indicate an increase by 7.7% in emissions and by 27.21% in total losses, demonstrating the superiority of the proposed strategy in minimizing emissions during the power dispatch between MGs and optimally adjusting the droop control coefficients as primary control objective.

A significant aspect to study is the precise impact of secondary control. For this purpose, the performance indices for frequency control are calculated, including MRE, ITAE, ITSE, IAE and ISE. The results demonstrate that a hierarchical control strategy without a secondary control is feasible. However, MOPSO control with a supervisory secondary control yields improved performance across all considered indices. Table 4 presents a numerical comparison of these indices.

5.3. Comparison against fmincon optimization

To demonstrate the capability of the proposed MOPSO algorithm in attaining optimal operational results, this section presents a performance comparison between the MOPSO-based strategy and a traditional nonlinear optimization technique carried out using the fmincon solver.

The fmincon function is a gradient-driven optimization tool designed for solving nonlinear problems. It minimizes a scalar objective function while adhering to both equality and inequality constraints—linear and nonlinear—as well as upper and lower limits on the decision variables. It relies on several numerical optimization strategies, including interior-point algorithms, sequential quadratic programming, and trust-region reflective methods, to find local solutions in problems where the objective and constraint functions are continuous and differentiable.

The formulation used for the fmincon method is detailed in Table 5.

Fig. 11 presents the results of the multi-objective optimization performed using the fmincon algorithm. Specifically, Fig. 11a illustrates the power distribution among the three MGs, ensuring full demand coverage at all times. For instance, at t=600 s, the allocated power values are P1=420 kW, P2=80 kW, and P3=280 kW, totaling a demand of 780 kW. In contrast, the power sharing determined by the MOPSO-based approach differs notably, with P1=260 kW, P2=220 kW, and P3=300 kW. This variation in power allocation directly influences system performance, enabling the MOPSO method to achieve superior results in terms of emissions and operational costs.

Fig. 11b depicts the objective function values corresponding to CO_2 emissions. The average emission value for the fmincon method is 8.58 T of CO_2, which corresponds to an increase of 3.5% compared to the MOPSO-proposed method, which achieves an average of 8.28 T of CO_2. This highlights the enhanced environmental efficiency of the MOPSO-based strategy. Furthermore, Fig. 11c shows the objective function related to power losses. The mean losses for fmincon amount to 1807 W, representing a 22.92% increase relative to the 1470 W average losses obtained via MOPSO. These results further corroborate the improved energy efficiency achieved by the MOPSO optimization. When comparing fmincon with the proportional power-sharing strategy, noticeable improvements are also evident: emissions are reduced from 8.92 T to 8.58 T of CO2 (a 3.96% decrease), and losses decrease from

Table 4
Frequency control comparison.

1	MOPSO control	Hierarchical Control	Variation (%)
MRE	$-3.37\cdot10^{-8}$	$-3.37\cdot10^{-5}$	100.09
ITAE	3259	4558	28.5
ITSE	11.11	19.76	43.78
IAE	3.552	5.119	30.61
ISE	$1.15\cdot10^{-2}$	$2.19\cdot10^{-2}$	47.72

Table 5
fmincon algorithm sequence.

Step	Procedure
1	Define objective function: $M.O.F = \min(w_1 \cdot OF_1 + w_2 \cdot OF_2)$
2	Define decision variables and bounds: $x = [P_{MG\ 1-2}\ ,\ P_{MG\ 3},\ n_1, n_2, (t_1), \ldots P_{MG\ 1-2}\ ,\ P_{MG\ 3},\ n_1, n_2, (t_1)(t_n)]$ with $0 \le P_{MG\ 1-2} \le P^{rated}_{MG\ 1-2}$, $0 \le P_{MG,3} \le P^{rated}_{MG\ 3}$, $0.01 \le n_1 \le 0.08$, $0.01 \le n_2 \le 0.08$,
3	Specify constraints: $c(x) \le 0$
4	Set the initial solution vector x_0 as the starting estimate for $P_{MG\ 1-2}$, $P_{MG\ 3}$, n_1, n_2 across the time interval T
5	Utilize a nonlinear optimization algorithm to progressively reduce the objective function, while respecting all imposed constraints and variable limits, and updating x until the convergence conditions are satisfied
6	Obtain the optimal power profile x_{opt} that results in the lowest $M.O.F$ value, and confirm the validity and effectiveness of the solution by means of simulation or experimental assessment.

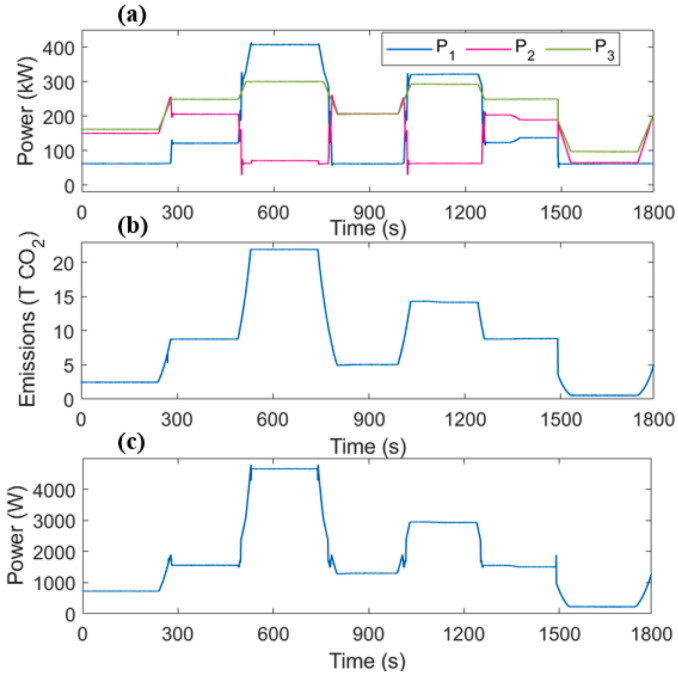

Fig. 11. fmincon optimization: (a) MGs power: P_1, P_2 and P_3, (b) CO_2 emissions and (c) power losses.

1.87 kW to 1.807 kW (a 3.48% decrease). This demonstrates that fmincon can enhance the baseline proportional distribution method. However, among all three strategies evaluated, the MOPSO-based approach consistently delivers the best overall performance in terms of emissions reduction and power losses. Table 6 summarizes the comparative quantitative results for emissions and losses across the three strategies, clearly confirming the superior performance of the proposed MOPSO-based multi-objective optimization in the energy management of IMGCs.

5.4. MOPSO under fault operation

One of the key considerations in designing control schemes for IMGCs is their resilience to faults. This section demonstrates the fault resilience of the hierarchical MOPSO control. Fig. 12 presents a simulation in which a fault in the converter of MG_2 is considered.

Fig. 12a shows the total active power, P_{TOTAL}, and the power values for each MG. At t=5 s, the demand increases from 300 kW to 375 kW, causing a sharp drop in frequency to 59.87 Hz (Fig. 12b), and a reduction in voltage to 593.1 V (Fig. 12c). Subsequently, a fault occurs in MG_2 at t=15 s. As a result, MG_2 is isolated from the IMGC, and P_2 is set to 0. To maintain the demand, P_1 increases from 113.9 kW to 215.6 kW, while the control of MG_3 remains independent, maintaining a power output of 160 kW before and after the fault.

Fig. 12b illustrates that the frequency decreases due to the fault, reaching a value of 59.79 Hz, which remains above the minimum threshold of 59.7 Hz. Similarly, Fig. 12c shows an increase in voltage to 582.1 V, which stays within the minimum acceptable range of 576 V. Finally, as a consequence of the fault, the IMGC system operator decides to reduce the demand from 374 kW to 253 kW at 20 s. The IMGC responds appropriately, maintaining P_1=143 kW, P_2=0 kW, and P_3 =110 kW. The frequency increases to 60.17 Hz, within the maximum threshold of 60.3 Hz. The voltage rises to 622.8V as the demand decreases, remaining within the maximum voltage threshold of 624 V.

5.5. Performance under communication delay

In addition to electrical faults that may disrupt power supply, it is crucial to maintain a reliable communication system to ensure proper operation despite inevitable communication delays. In simulation studies and HIL validations, the following standard delay ranges are typically considered to characterize communication latency [46]: low delays (1–10 ms), suitable for real-time primary and secondary distributed control; medium delays (10–100 ms), common in centralized or EMS coordination and tertiary control schemes or MG-to-MG exchanges; and high delays (greater than 100 ms), often used to evaluate robustness under fault or network congestion conditions.

In this section, the fault scenario detailed in Section 5.4 is subjected to three communication delay profiles—low (1 ms), medium (10 ms), and high (100 ms)—to rigorously assess the robustness of the proposed IMGC under simultaneous electrical faults and communication latency.

Fig. 13 presents the frequency and voltage control responses of the IMGC when MG_2 experiences a fault under varying communication delays. For the low-delay case of 1 ms, Fig. 13a shows frequency values nearly identical to those obtained in the ideal, no-delay scenario, demonstrating that the system's dynamic response remains virtually unaffected by minimal latency. Similarly, the voltage profile in Fig. 13d exhibits maximum and minimum disturbances closely matching those of the no-delay case, confirming stable voltage regulation under low-latency conditions.

When considering medium delays of 10 ms, Fig. 13b and Fig. 13e illustrate a noticeable increase in deviation from the ideal response. Frequency disturbances reach maxima of 59.84 Hz and minima of 59.76 Hz, compared to 59.87 Hz and 59.79 Hz in the baseline case. Voltage also exhibits greater fluctuations, peaking at approximately 624 V; nevertheless, voltage remains well-regulated and stable throughout the simulation window.

Finally, Fig. 13c and Fig. 13f depict the system's behavior under the most challenging delay scenario of 100 ms. Here, both frequency and voltage exhibit more perturbations, reflecting the increased difficulty posed by such latency. Despite this, the IMGC maintains system stability, ensuring that frequency and voltage remain within acceptable thresholds (59.76 Hz and 624 V, respectively).

These findings conclusively demonstrate that even under extreme conditions—combining an electrical fault in one MG with varying communication delays—the MOPSO-based control strategy embedded in the IMGC preserves stability and effective regulation. This robust performance underscores the capability of the proposed controller to handle real-world operational challenges, ensuring resilient and reliable MG operation despite the uncertainties introduced by communication network imperfections.

Table 6
Comparison of the control methods.

Symbol	MOPSO control	fmincon Control	Hierarchical Control
E_{avg}^{opt} (T CO_2)	8.28	8.58 (+3.96 %)	8.92 (+7.7 %)
P_{avg}^{opt} (W)	1470	1807 (+22.92%)	1870 (+27.21%)

5.6. Hardware-in-the-loop experimental validation

This section demonstrates the practical implementation of the proposed hierarchical MOPSO control within a HIL setup. For this, an OPAL-RT4512 unit is used to run the plant in real-time. The OPAL-RT4512 device is managed through the RT-Lab software, which enables programming and real-time monitoring of the plant. Powered by four powerful 3.7 GHz cores, the plant runs with a time step of 50 μs.

The MOPSO is executed on a dSPACE MicroLabBox controller, which sends the reference values for $P_{MG,1-2}$, $P_{MG,3}$, $n_{1,opt}$, and $n_{2,opt}$ to the OPAL-RT4512 unit. This communication is carried out using a set of analog inputs and outputs with a voltage range of +16V/-16V. Finally, the results are displayed on a DLM4038 digital oscilloscope. Fig. 14 shows the configuration of the experimental setup, comprising a host PC with RT-Lab, the OPAL-RT4512 device, the dSPACE MicroLabBox controller, the set of analog input-output cards, and the DLM4038 oscilloscope.

Fig. 15 shows a 50 s real-time simulation illustrating the variations in both active and reactive power demand, showing variations in active and reactive power demand. Fig. 15a displays the experimental measurements of P_{PCC} (blue signal) and Q_{PCC} (green signal). For accurate representation, the signals are plotted with a horizontal scale of 5 s/div and a vertical scale of 1 V/div. For instance, at t=10s, the P_{PCC} measurement of 5.5 V corresponds to 550 kW. Similarly, at t=25 s, the Q_{PCC} measurement of 1.85 V represents 185 kVAr.

Figs. 15b and 15c show the experimentally measured values of active and reactive power for each MG, respectively. Fig. 15b is plotted with a scale of 5 s/div and 1 V/div. The power values are represented in per unit (pu), amplified by a factor of 5 for better visualization. The base power for $P_{MG,1-2}$ is 500 kVA, and the base power for $P_{MG,3}$ is 300 kVA. At t=10 s, P_1 (blue signal) measures 0.75 V (0.15 pu), equivalent to 75 kW. P_2 (purple signal) is 2.35 V (0.47 pu), corresponding to 235 kW.

Finally, for P_3 (green signal), the measurement is 4 V (0.8 pu), equivalent to 240 kW, completing the active power balance. Fig. 15c is plotted with a scale of 5 s/div and 0.375 V/div. At t=25 s, Q_1 (blue signal) measures 0.83V (0.167 pu), corresponding to 83.6 kVAr. Meanwhile, Q_2 (purple signal) is 1.014 V (0.203 pu), corresponding to 101.4 kVAr, and Q_3 (green signal) remains at 0 V, completing the total reactive power balance of 185 kVAr.

Figs. 15d and 15e show the measured frequency (f_{PCC}) and voltage (V_{PCC}) values at the PCC. In Fig. 15d, the signal is scaled by a factor of 10

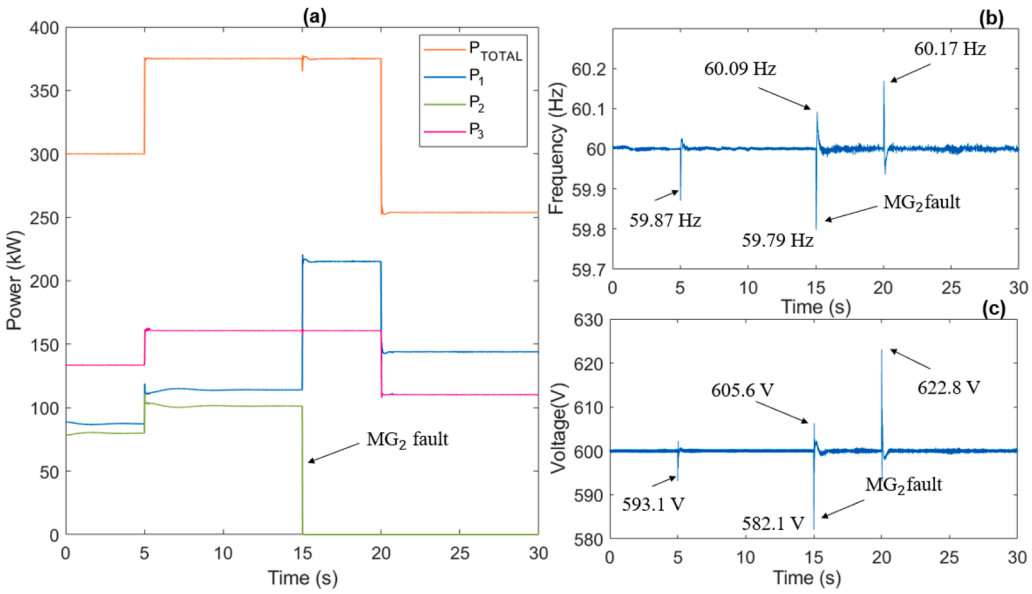

Fig. 12. MOPSO control under failure: (a) Total power (P_{TOTAL}) and power of each MG (P_i), (b) IGMC frequency, and (c) IGMC voltage.

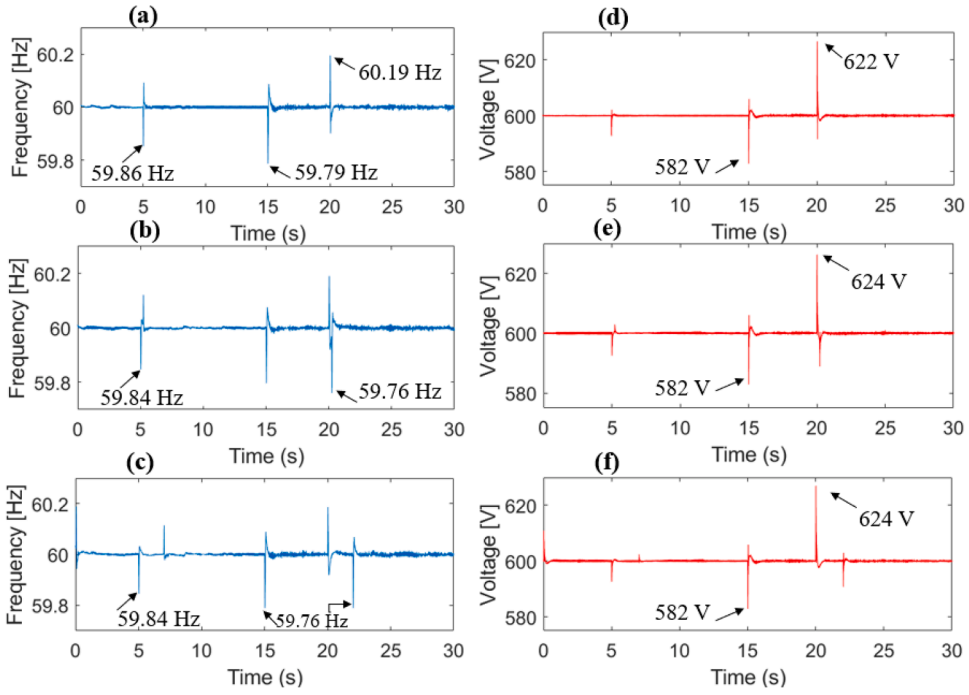

Fig. 13. IMGC under communication delay: (a) frequency under 1 ms delay, (b) frequency under 10 ms delay, (c) frequency under 100 ms delay, (d) voltage under 1 ms delay, (e) voltage under 10 ms delay, (f) voltage under 100 ms delay.

with a horizontal axis of 5s/div and a vertical scale of 0.5V/div. A measured value of 6V corresponds to a frequency of 60 Hz throughout the simulation. Similarly, in Fig. 15e, the signal is scaled by a factor of 100, using the same axis scales. The measured signal of 6V corresponds to 600V at the PCC. The experimental results validate, on one hand, the real-time performance and reproducibility of the proposed MOPSO-based hierarchical control, and on the other hand, verify the finding obtained from MATLAB/Simulink simulations, demonstrating the practical applicability of the proposed approach.

6. Conclusions

This paper presented an optimal hierarchical control for an IMGC, based on the real-time implementation of a MOPSO algorithm. This algorithm enabled optimal energy distribution between MGs and the optimization of operation within each MG. The main contribution of this research lay in the capability of the MOPSO algorithm to simultaneously integrate the optimization of CO_2 emissions as a tertiary control objective and the minimization of total losses as a primary control objective. The proposed IMGC employed a combination of GS and GF inverters to interconnect the MGs. It was demonstrated that a rigorous analytical framework can be developed to establish the total losses of an IMGC

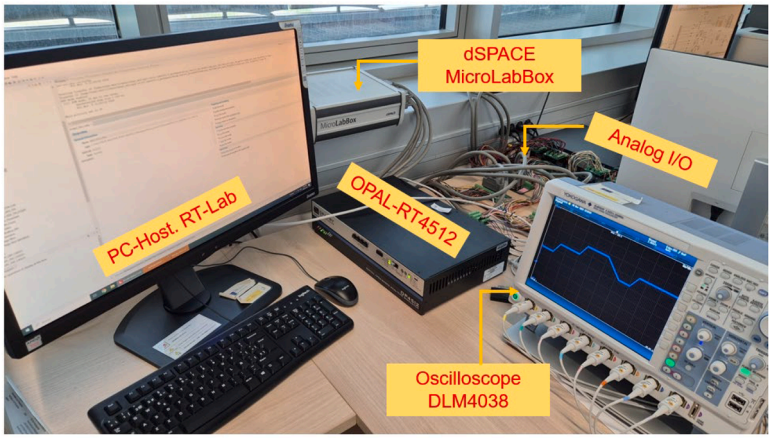

Fig. 14. Experimental HIL setup formed by OPAL-RT4512, dSPACE MicroLabBox, Oscilloscope DLM4038 and PC-Host.

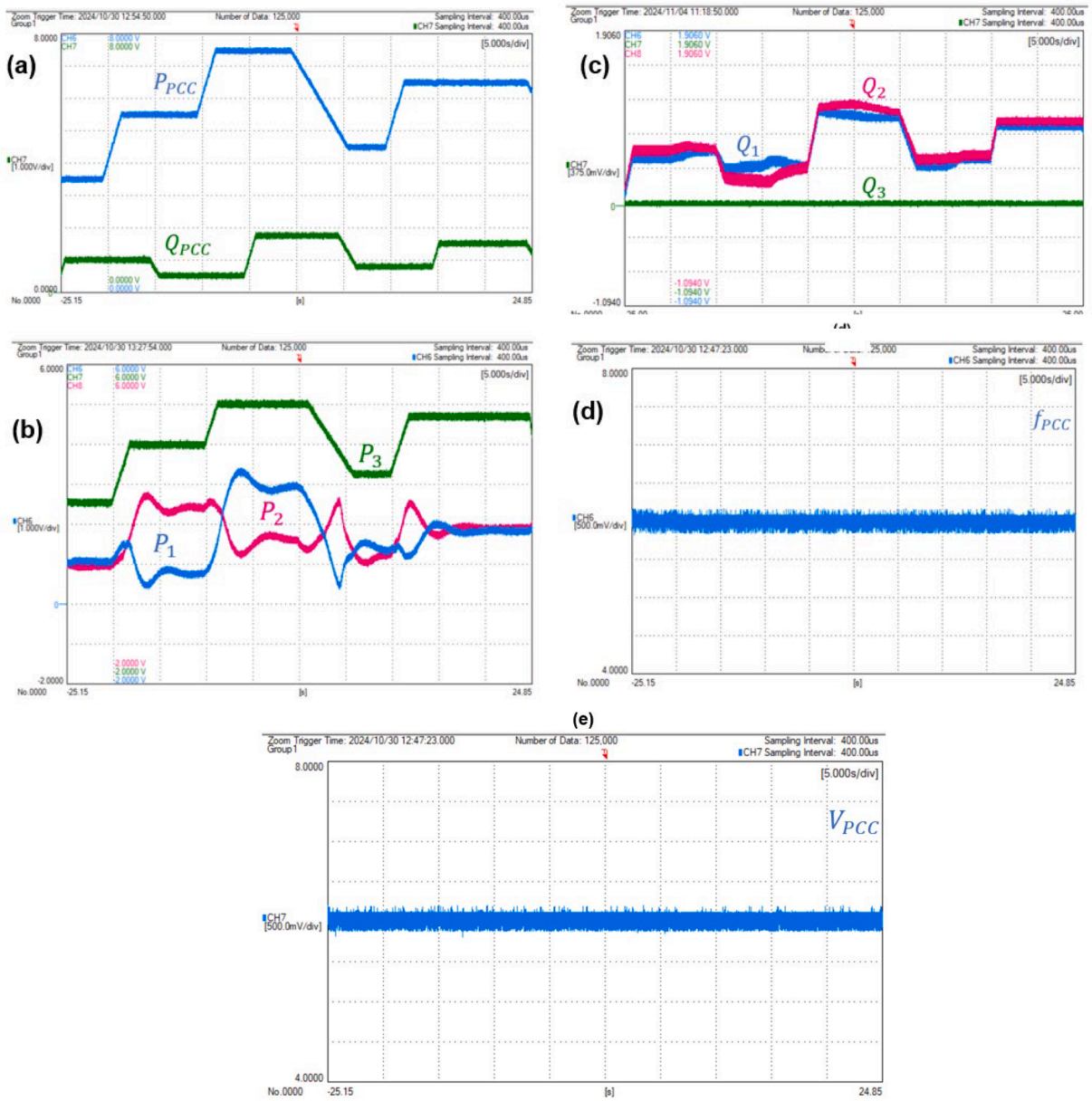

Fig. 15. Experimental results: (a) Active (P_{PCC}) and reactive power (Q_{PCC}) at PCC, (b) MGs active power (P_i), (c) MGs reactive power (Q_i), (d) frequency at PCC (f_{PCC}) and (e) voltage at PCC (V_{PCC}).

solely based on the droop control coefficients used in the primary control and the frequencies required for their contribution. By employing general measures within the IMGC, such as the droop control coefficients and frequency measurements, this approach is flexible and easily adaptable for further MGC studies. The effectiveness of the MOPSO-based hierarchical control was validated across multiple scenarios, with experimental results demonstrating a 21.37% reduction in total losses and a 7.66% decrease in CO2 emissions compared to a traditional proportional approach. Additionally, when compared with an optimization based on the fmincon solver, the proposed method achieved a 22.92% reduction in losses and a 3.5% decrease in emissions. These results highlight not only the advantage of employing an advanced hierarchical approach but also how real-time optimization can lead to significant improvements in energy efficiency and sustainability. The implementation of centralized secondary control in this study led to significant improvements in performance indices, including a 100.09% improvement in MRE, 28.5% in ITAE, 43.78% in ITSE, 30.61% in IAE, and 47.72% in ISE, demonstrating that the MOPSO-based hierarchical approach is not only more efficient in terms of reducing losses and emissions but also enhances the stability and control of the IMGC. The robustness and flexibility of the MOPSO were validated in scenarios involving MG failures and unexpected changes in active and reactive power demand. The results demonstrated that the system's ability to adapt effectively, maintaining frequency and voltage stability within the predefined limits. This not only highlights the MOPSO's adaptability to contingencies but also underscores the applicability of the proposed algorithm in real-world, dynamic situations, emphasizing the practical and operational value of this research. Furthermore, the practical feasibility of the proposed approach was further confirmed through HIL experimentation using an OPAL-RT4512 unit and a dSPACE MicroLabBox controller. The experimental results, with a sampling time of 50 μs, closely aligned with the simulation results, demonstrating the effectiveness of the real-time control implementation. Future investigations could include incorporating coarse-grained modeling strategies, such as granular computing approaches, to enhance the accuracy and efficiency of the optimization process. In particular, granular-ball computing could be explored as a method to structure high-dimensional data spaces and manage uncertainty in system operation by dynamically grouping input features into adaptive spherical granules. This approach would facilitate a more efficient exploration of the solution space by the MOPSO algorithm, especially under conditions of noise or partial observability. Furthermore, combining granular-ball computing with neighbourhood rough sets or three-way decision models may offer a robust framework for classifying MG operating states and supporting real-time control decisions in complex and uncertain environments.

CRediT authorship contribution statement

Pablo Horrillo-Quintero: Writing – original draft, Visualization, Validation, Software, Resources, Methodology, Investigation, Formal analysis, Data curation, Conceptualization. **Pablo García-Triviño:** Writing – original draft, Visualization, Validation, Software, Resources, Methodology, Investigation, Conceptualization. **David Carrasco-González:** Writing – original draft, Methodology, Investigation, Formal analysis, Conceptualization. **Raúl Sarrias-Mena:** Writing – original draft, Methodology, Investigation, Formal analysis, Conceptualization. **Marcos Tostado:** Writing – original draft, Methodology, Investigation, Formal analysis, Conceptualization. **Francisco Jurado:** Writing – review & editing, Supervision, Project administration, Investigation, Funding acquisition, Conceptualization. **Luis Sainz Sapera:** Writing – review & editing, Supervision, Project administration, Methodology, Investigation, Funding acquisition, Conceptualization. **Luis M. Fernández-Ramírez:** Writing – review & editing, Visualization, Validation, Supervision, Project administration, Methodology, Investigation, Funding acquisition, Conceptualization.

Declaration of competing interest

The authors declare that they have no known competing financial interests or personal relationships that could have appeared to influence the work reported in this paper.

Acknowledgments

This work was partially supported by Ministerio de Ciencia e Innovación, Agencia Estatal de Investigación, FEDER, UE (Grants PID2021-123633OB-C31, PID2021-123633OB-C32 and PID2021-123633OB-C33 supported by MCIN/AEI/10.13039/501100011033/ FEDER, UE).

Data availability

Data will be made available on request.

References

[1] M. Mazidi, N. Rezaei, F.J. Ardakani, M. Mohiti, JM. Guerrero, A hierarchical energy management system for islanded multi-microgrid clusters considering frequency security constraints, Int. J. Electr. Power Energy Syst. 121 (2020), https://doi.org/10.1016/j.ijepes.2020.106134.
[2] M. Zhang, Y. Li, F. Liu, W.J. Lee, Y. Peng, Y. Liu, et al., A robust distributed secondary voltage control method for islanded microgrids, Int. J. Electr. Power Energy Syst. 121 (2020), https://doi.org/10.1016/j.ijepes.2020.105938.
[3] B. Long, Y. Liao, K.T. Chong, J. Rodríguez, JM. Guerrero, MPC-Controlled Virtual Synchronous Generator to Enhance Frequency and Voltage Dynamic Performance in Islanded Microgrids, IEEe Trans. Smart. Grid. 12 (2021) 953–964, https://doi.org/10.1109/TSG.2020.3027051.
[4] M. Basu, Dynamic optimal power flow for isolated microgrid incorporating renewable energy sources, Energy 264 (2023), https://doi.org/10.1016/j.energy.2022.126065.
[5] N. Wu, J. Xu, J. Linghu, J. Huang, Real-time optimal control and dispatching strategy of multi-microgrid energy based on storage collaborative, Int. J. Electr. Power Energy Syst. 160 (2024), https://doi.org/10.1016/j.ijepes.2024.110063.
[6] N.K. Sifakis, FD. Kanellos, Real-Time Multi-Agent Based Power Management of Virtually Integrated Microgrids Comprising Prosumers of Plug-in Electric Vehicles and Renewable Energy Sources, IEEe Access. 12 (2024) 161842–161865, https://doi.org/10.1109/ACCESS.2024.3490434.
[7] M.H. Elkholy, M. Elymany, H. Metwally, M.A. Farahat, T. Senjyu, M. Elsayed Lotfy, Design and implementation of a Real-time energy management system for an isolated Microgrid: Experimental validation, Appl. Energy 327 (2022), https://doi.org/10.1016/j.apenergy.2022.120105.
[8] K.B. Han, J. Jung, BO. Kang, Real-time load variability control using energy storage system for demand-side management in South Korea, Energies. (Basel) 14 (2021), https://doi.org/10.3390/en14196292.
[9] H.S. Fesagandis, M. Jalali, K. Zare, M. Abapour, H. Karimipour, Resilient Scheduling of Networked Microgrids against Real-Time Failures, IEEe Access. 9 (2021) 21443–21456, https://doi.org/10.1109/ACCESS.2021.3052653.
[10] Q. Xu, Y. Xu, Z. Xu, L. Xie, F. Blaabjerg, A Hierarchically Coordinated Operation and Control Scheme for DC Microgrid Clusters under Uncertainty, IEEe Trans. Sustain. Energy 12 (2021) 273–283, https://doi.org/10.1109/TSTE.2020.2991096.
[11] Z.H.A. Al-Tameemi, T.T. Lie, G. Foo, F. Blaabjerg, Control strategies of DC microgrids cluster: A comprehensive review, Energies. (Basel) 14 (2021), https://doi.org/10.3390/en14227569.
[12] X. Wu, Y. Xu, J. He, X. Wang, J.C. Vasquez, JM. Guerrero, Pinning-Based Hierarchical and Distributed Cooperative Control for AC Microgrid Clusters, IEEe Trans. Power. Electron. 35 (2020) 9867–9887, https://doi.org/10.1109/TPEL.2020.2972321.
[13] K.W. Lao, W. Deng, J. Sheng, N. Dai, PQ-Coupling Strategy for Droop Control in Grid-Connected Capacitive-Coupled Inverter, IEEe Access. 7 (2019) 31663–31671, https://doi.org/10.1109/ACCESS.2019.2902314.
[14] B. Alghamdi, CA. Cañizares, Frequency Regulation in Isolated Microgrids through Optimal Droop Gain and Voltage Control, IEEe Trans. Smart. Grid. 12 (2021) 988–998, https://doi.org/10.1109/TSG.2020.3028472.
[15] M.Q. Taha, S. Kurnaz, Droop Control Optimization for Improved Power Sharing, AC Islanded Microgrids Based on Centripetal Force Gravity Search Algorithm. Energies (Basel) 16 (2023), https://doi.org/10.3390/en16247953.
[16] M. Veysi, J. Aghaei, M.R. Soltanpour, M. Shasadeghi, B. Bahrani, DJ. Ryan, Robust, Accurate, and Fast Decentralized Power Sharing Mechanism for Isolated DC Microgrid Using Droop-Based Sliding-Mode Control, IEEe Trans. Smart. Grid. 13 (2022) 4160–4173, https://doi.org/10.1109/TSG.2022.3181494.
[17] J.W. Simpson-Porco, Q. Shafiee, F. Dorfler, J.C. Vasquez, J.M. Guerrero, F. Bullo, Secondary Frequency and Voltage Control of Islanded Microgrids via Distributed Averaging, IEEE Transac. Industr. Electr. 62 (2015) 7025–7038, https://doi.org/10.1109/TIE.2015.2436879.

[18] M.A. Hartani, H. Rezk, A. Benhammou, M. Hamouda, O. Abdelkhalek, S. Mekhilef, et al., Proposed frequency decoupling-based fuzzy logic control for power allocation and state-of-charge recovery of hybrid energy storage systems adopting multi-level energy management for multi-DC-microgrids, Energy 278 (2023), https://doi.org/10.1016/j.energy.2023.127703.
[19] M. Zaery, P. Wang, W. Wang, D. Xu, Distributed Global Economical Load Sharing for a Cluster of DC Microgrids, IEEE Transac. Power Syst. 35 (2020) 3410–3420, https://doi.org/10.1109/TPWRS.2020.2975378.
[20] M.A. Hoummadi, H.A. Aroussi, B. Bossoufi, M. Karim, Constraints and Adjustable Parameters in Microgrids for Cost and CO2 Emission Reduction, in: Proceedings of the 16th International Conference on Electronics, Computers and Artificial Intelligence, ECAI 2024, Institute of Electrical and Electronics Engineers Inc., 2024, https://doi.org/10.1109/ECAI61503.2024.10607579.
[21] D. Arcos–Aviles, A. Salazar, M. Rodriguez, W. Martinez, F. Guinjoan, Model predictive control-based energy management system for an isolated electro-thermal microgrid in the Amazon region of Ecuador, Energy Convers. Manage 310 (2024), https://doi.org/10.1016/j.enconman.2024.118479.
[22] S. Yadav, P. Kumar, A. Kumar, Excess energy management and techno-economic analysis of optimal designed isolated microgrid with reliability and environmental aspects, Energy Convers. Manage 333 (2025), https://doi.org/10.1016/j.enconman.2025.119772.
[23] M. Huylo, S. Taheri, A. Novoselac, Integration of renewable energy generation and storage systems for emissions reduction in an islanded campus microgrid, Build. Environ. 274 (2025), https://doi.org/10.1016/j.buildenv.2025.112736.
[24] X. Zhou, Q. Ai, H. Wang, Adaptive marginal costs-based distributed economic control of microgrid clusters considering line loss, Energies. (Basel) 10 (2017), https://doi.org/10.3390/en10122071.
[25] Y. Jiang, Y. Yang, S.C. Tan, SYR. Hui, Power Loss Minimization of Parallel-Connected Distributed Energy Resources in DC Microgrids Using a Distributed Gradient Algorithm-Based Hierarchical Control, IEEe Trans. Smart. Grid. 13 (2022) 4538–4550, https://doi.org/10.1109/TSG.2022.3185264.
[26] Z. Belboul, B. Toual, A. Kouzou, L. Mokrani, A. Bensalem, R. Kennel, et al., Multiobjective Optimization of a Hybrid PV/Wind/Battery/Diesel Generator System Integrated in Microgrid: A Case Study in Djelfa, Algeria. Energies (Basel) 15 (2022), https://doi.org/10.3390/en15103579.
[27] X. Zhu, C. Peng, H. Geng, Multi-Objective Sizing Optimization Method of Microgrid Considering Cost and Carbon Emissions. 2022 4th International Conference on Smart Power and Internet Energy Systems, SPIES 2022, Institute of Electrical and Electronics Engineers Inc., 2022, pp. 2278–2283, https://doi.org/10.1109/SPIES55999.2022.10082041.
[28] R. Yang, G. Shen, Alahmed AS, Fan C, Co-Optimizing Distributed Energy Resources under Demand Charges and Bi-Directional Power Flow (2025).
[29] I. Nordin, K. Elofsson, T. Jansson, Cost-effective reductions in greenhouse gas emissions: Reducing fuel consumption or replacing fossil fuels with biofuels, Energy Policy 190 (2024), https://doi.org/10.1016/j.enpol.2024.114138.
[30] J. Yang, Z. Liu, G. Wang, Q. Zhang, S. Xia, D. Wu, et al., Constructing Three-Way Decision With Fuzzy Granular-Ball Rough Sets Based on Uncertainty Invariance, IEEE Transac. Fuzzy Syst. 33 (2025) 1781–1792, https://doi.org/10.1109/TFUZZ.2025.3536564.
[31] Z. Jia, Z. Zhang, W. Pedrycz, Generation of Granular-Balls for Clustering Based on the Principle of Justifiable Granularity, IEEe Trans. Cybern. 55 (2025) 1687–1700, https://doi.org/10.1109/TCYB.2025.3534195.
[32] S. Anttila, J.S. Döhler, J.G. Oliveira, C. Boström, Grid Forming Inverters: A Review of the State of the Art of Key Elements for Microgrid Operation, Energies. (Basel) 15 (2022), https://doi.org/10.3390/en15155517.
[33] Z. Liu, J. Yang, Y. Zhang, T. Ji, J. Zhou, Z. Cai, Multi-Objective Coordinated Planning of Active-Reactive Power Resources for Decentralized Droop-Controlled Islanded Microgrids Based on Probabilistic Load Flow, IEEe Access. 6 (2018) 40267–40280, https://doi.org/10.1109/ACCESS.2018.2855697.
[34] X. Lu, J. Lai, X. Yu, Y. Wang, JM. Guerrero, Distributed coordination of islanded microgrid clusters using a two-layer intermittent communication network, IEEe Trans. Industr. Inform. 14 (2018) 3956–3969, https://doi.org/10.1109/TII.2017.2783334.
[35] J. Lai, X. Lu, X. Yu, A. Monti, Cluster-Oriented Distributed Cooperative Control for Multiple AC Microgrids, IEEe Trans. Industr. Inform. 15 (2019) 5906–5918, https://doi.org/10.1109/TII.2019.2908666.
[36] L. Huang, W. Sun, Q. Li, D. Mu, W. Li, A two-layer energy management for islanded microgrid based on inverse reinforcement learning and distributed ADMM, Energy 301 (2024), https://doi.org/10.1016/j.energy.2024.131672.
[37] M.T. Kuo, Lu S Der, M.C. Tsou, Considering Carbon Emissions in Economic Dispatch Planning for Isolated Power Systems: A Case Study of the Taiwan Power System, IEEe Trans. Ind. Appl. 54 (2018) 987–997, https://doi.org/10.1109/TIA.2017.2771338.
[38] K. Selvakumar, D. Selvabharathi, R. Palanisamy, T.M. Thamizh Thentral, CO2Emission-Constrained Short-Term Unit Commitment Problem Using Shuffled Frog Leaping Algorithm, J. Electr. Computer Eng. (2023), https://doi.org/10.1155/2023/2336689, 2023.
[39] MI. Alomoush, Microgrid dynamic combined power–heat economic-emission dispatch with deferrable loads and price-based energy storage elements and power exchange, Sustain. Energy, Grids Netw. 26 (2021), https://doi.org/10.1016/j.segan.2021.100479.
[40] J. Ma, L. Yuan, Z. Zhao, F. He, Transmission Loss Optimization-Based Optimal Power Flow Strategy by Hierarchical Control for DC Microgrids, IEEe Trans. Power. Electron. 32 (2017) 1952–1963, https://doi.org/10.1109/TPEL.2016.2561301.
[41] X. Zheng, Q. Li, J. Yuan, Z. Chen, Distributed Weighted Gradient Descent Method with Adaptive Step Sizes for Energy Management of Microgrids, IEEe Trans. Smart. Grid. 15 (2024) 4436–4449, https://doi.org/10.1109/TSG.2024.3400982.
[42] Z.H.A. Al-Tameemi, T.T. Lie, G. Foo, F. Blaabjerg, Optimal Coordinated Control of DC Microgrid Based on Hybrid PSO–GWO Algorithm †, Electricity 3 (2022) 346–364, https://doi.org/10.3390/electricity3030019.
[43] R. Zheng, Y. Zhang, X. Sun, F. Wang, L. Yang, C. Peng, et al., Multi-objective particle swarm optimisation of complex product change plan considering service performance, CAAI. Trans. Intell. Technol. 8 (2023) 1058–1076, https://doi.org/10.1049/cit2.12176.
[44] S. Talebi, HH. Aly, Optimized Renewable Energy Integration: Advanced Modeling, Control, and Design of a Standalone Microgrid Using Hybrid FA-PSO, IEEe Access. 13 (2025) 63486–63503, https://doi.org/10.1109/ACCESS.2025.3559725.
[45] C. Keerthisinghe and D. S. Kirschen, "Real-Time Digital Simulation of Microgrid Control Strategies," 2020 IEEE Power & Energy Society Innovative Smart Grid Technologies Conference (ISGT), Washington, DC, USA, 2020, pp. 1-5, doi: 10.1109/ISGT45199.2020.9087709.
[46] A. Kondoro, Dhaou I Ben, H. Tenhunen, N. Mvungi, A low latency secure communication architecture for microgrid control, Energies. (Basel) 14 (2021), https://doi.org/10.3390/en14196262.